ESC European Society of Cardiology

Cardiovascular Research (2024) **00**, 1–16
https://doi.org/10.1093/cvr/cvae186

Single-cell analysis reveals the implication of vascular endothelial cell-intrinsic *ANGPT2* in human intracranial aneurysm

Guo Yu[1,3,4,5,6†], Jia Li[2†], Hongfei Zhang[1,3,4,5,6†], Huaxing Zi[2,7], Mingjian Liu[1,3,4,5,6], Qingzhu An[1,3,4,5,6], Tianming Qiu[1,3,4,5,6], Peiliang Li[1,3,4,5,6], Jianping Song [1,3,4,5,6], Peixi Liu[1,3,4,5,6], Kai Quan[1,3,4,5,6], Sichen Li[1,3,4,5,6], Yingjun Liu[1,3,4,5,6], Wei Zhu[1,3,4,5,6]*, and Jiulin Du [2,7,8]*

[1]Department of Neurosurgery, Huashan Hospital, Shanghai Medical College, Fudan University, 12 Middle Wulumuqi Road, Shanghai 200040, China; [2]Institute of Neuroscience, State Key Laboratory of Neuroscience, CAS Center for Excellence in Brain Science and Intelligence Technology, Chinese Academy of Sciences, 320 Yueyang Road, Shanghai 200031, China; [3]National Center for Neurological Disorders, 12 Middle Wulumuqi Road, Shanghai 200040, China; [4]Shanghai Key Laboratory of Brain Function and Restoration and Neural Regeneration, 12 Middle Wulumuqi Road, Shanghai 200040, China; [5]Neurosurgical Institute of Fudan University, 12 Middle Wulumuqi Road,Shanghai 200040, China; [6]Shanghai Clinical Medical Center of Neurosurgery,12 Middle Wulumuqi Road, Shanghai 200040, China; [7]University of Chinese Academy of Sciences, 19A Yu-Quan Road, Beijing 100049, China; and [8]School of Life Science and Technology, ShanghaiTech University, 319 Yue-Yang Road, Shanghai 200031, China

Received 15 February 2024; revised 4 May 2024; accepted 13 June 2024; online publish-ahead-of-print 24 August 2024

Time of primary review: 39 days

Aims

While previous single-cell RNA sequencing (scRNA-seq) studies have attempted to dissect intracranial aneurysm (IA), the primary molecular mechanism for IA pathogenesis remains unknown. Here, we uncovered the alterations of cellular compositions, especially the transcriptome changes of vascular endothelial cells (ECs), in human IA.

Methods and results

We performed scRNA-seq to compare the cell atlas of sporadic IA and the control artery. The transcriptomes of 43 462 cells were profiled for further analysis. In general, IA had increased immune cells (T/NK cells, B cells, myeloid cells, mast cells, neutrophils) and fewer vascular cells (ECs, vascular smooth muscle cells, and fibroblasts). Based on the obtained high-quantity and high-quality EC data, we found genes associated with angiogenesis in ECs from IA patients. By EC-specific expression of candidate genes *in vivo*, we observed the involvement of *angpt2a* in causing cerebral vascular abnormality. Furthermore, an IA zebrafish model mimicking the main features of human IA was generated through targeting *pdgfrb* gene, and knockdown of *angpt2a* alleviated the vascular dilation in the IA zebrafish model.

Conclusion

By performing a landscape view of the single-cell transcriptomes of IA and the control artery, we contribute to a deeper understanding of the cellular composition and the molecular changes of ECs in IA. The implication of angiogenic regulator *ANGPT2* in IA formation and progression, provides a novel potential therapeutical target for IA interventions.

* Corresponding authors. Tel: +8621 52887230, Fax: +8621 52887230, E-mail: drzhuwei@fudan.edu.cn; Tel: +8621 54921825, Fax: +8621 54921735, E-mail: forestdu@ion.ac.cn
† These authors contributed equally to the study.

Graphical Abstract

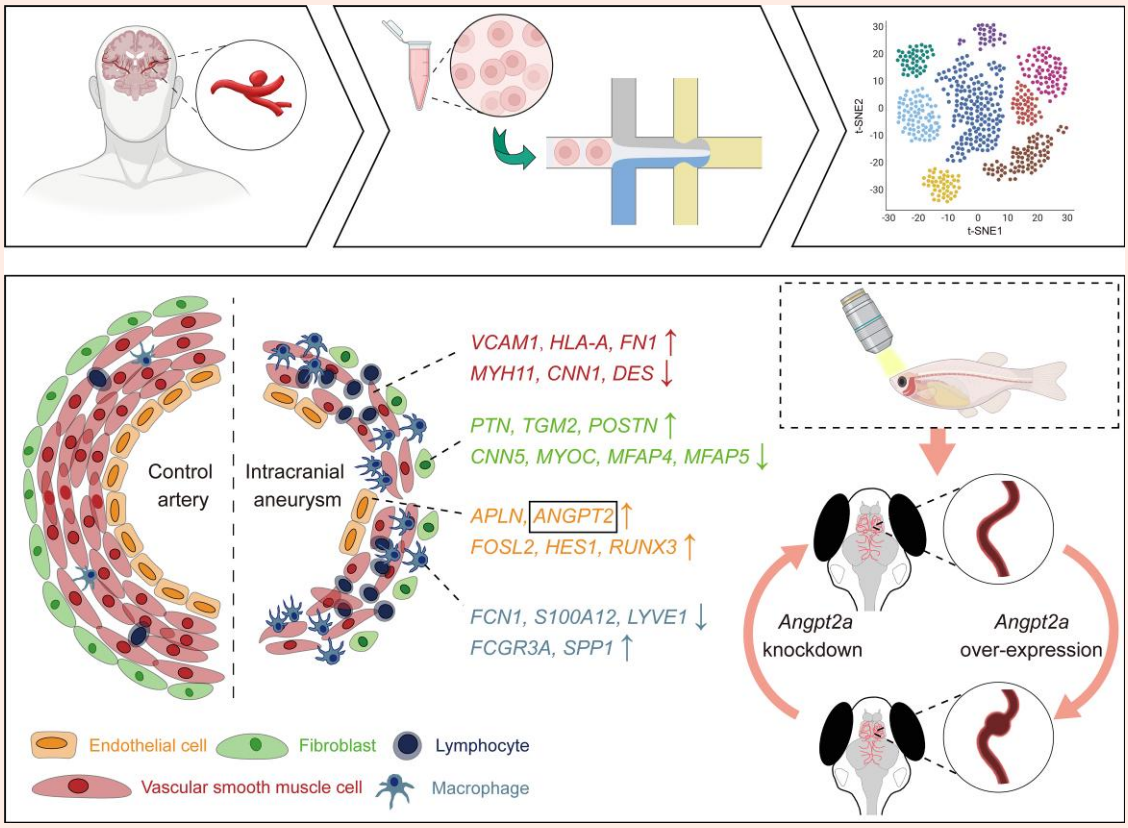

Keywords Single-cell RNA sequencing • Intracranial aneurysm • Endothelial cell • Heterogeneity

1. Introduction

Intracranial aneurysm (IA) is a focal bulging or ballooning in the cerebral arteries that affects 3.2% of the general population, with higher prevalence in elderly individuals.[1] Its rupture can lead to aneurysmal subarachnoid haemorrhage, a severe complication with a fatality rate of 27–44%.[2] Despite previous studies suggesting the involvement of various factors such as disturbed blood flow, vascular wall shear stress, oxidative stress, extracellular matrix degradation, and inflammation in IA formation and progression,[3,4] the underlying primary molecular mechanism remains poorly understood.

Single-cell RNA sequencing (scRNA-seq) is a cutting-edge approach that provides insight into the composition of different cell types and the identification of gene expression alterations at the single-cell level.[5,6] It has been applied to study the molecular and cellular mechanisms of human aneurysms.[7,8] Recent studies have primarily characterized the involvement of vascular smooth muscle cells (vSMCs) and macrophages/monocytes in the progression of elastase-induced IA in mouse models using single-cell transcriptomic profiling.[9] In a previous study, the single-cell landscape of human blood blister-like aneurysm was co-analysed with the saccular IA, which drew similar conclusions regarding the implication of vSMCs and macrophages.[10] However, a normal sample control was not included in that study, and the molecular changes of endothelial cell (ECs) in IA at the single-cell level have not yet been examined. Hence, the scRNA-seq analysis of human IA and the control arteries, especially the transcriptome changes of ECs at the single-cell level, remains an area of research that needs further investigation.

In the present study, we uncovered the cellular heterogeneity of human IA and the control artery by scRNA-seq. In addition to vSMC, fibroblasts and immune cells, we obtained the first high-quality and high-quantity EC data from IA patients. We found evidence of enhanced angiogenesis-related signalling pathways in ECs and identified candidate genes that were specific to ECs in IA. Using the zebrafish model, we screened those candidate genes and discovered that the angiogenic gene *angpt2a* is involved in causing IA-like vascular bulging in the brain. Furthermore, we created a novel genetic zebrafish model of IA that mimics the main features of human IAs and showed that inhibiting *angpt2a* could alleviate the artery dilation. These results deepen our understanding of the primary molecular changes in ECs that lead to IA, and highlight the role of EC-intrinsic *ANGPT2* in IA formation.

2. Methods

2.1 Patients and samples

The protocol for collecting human tissue samples was approved by the Research and Ethical Committee of Huashan Hospital, Fudan University (Protocol number KY2017-386), and complied with the Declaration of Helsinki. Written informed consent was obtained from all participants before enrolment. Sporadic patients with saccular IA were diagnosed by medical history and digital subtraction angiography. Patients were excluded if they had multiple aneurysms, dissecting aneurysm, family history of IA and/or subarachnoid haemorrhage, genetic predisposition (polycystic kidney disease, Type IV Ehlers-Danlos syndrome, Marfan syndrome, Loeys

Dietz syndrome), infection, or trauma. In total, three IA samples were dissected and obtained after the aneurysm neck was satisfied with surgical clipping. For control purpose, three superficial temporal arteries (STAs) samples were obtained from patients undergoing frontotemporal craniotomy for resecting intracranial tumours. And the detailed clinical characteristics were available in Supplementary material online, *Table S1*.

2.2 scRNA-seq library preparation

The fresh IA and STA tissue was minced on ice and dissociated with 0.25% Trypsin (Gibco, USA) and 0.2% collagenase type I (Gibco, USA) for 30 min at 37°C. Then the samples were filtered through a 40 μm cell strainer, centrifuged at 500 × *g* for 5 min, and discarded the supernatant. The cell pellet was resuspended with red blood cell lysis buffer (MACS, German) and incubated for 10 min. After centrifuging and decanting the supernatant, the cell pellet was washed and resuspended in RPMI 1640 (Corning, USA) containing 0.04% BSA (MACS, German). Then the single-cell gel beads in emulsions were generated by loading single-cell suspensions onto a Chromium Single Cell Controller Instrument (10× Genomics, USA). After that, reverse transcription, cDNA PCR amplification, and library preparation were performed as per manufacturer's directions. All libraries were sequenced using the Illumina NovaSeq 6000 with 2 × 150 bp paired-end reads.

2.3 scRNA-seq data processing

Raw sequencing data was processed by Cell Ranger software (10× genomics, version 5.0.0), including de-multiplexing cellular barcodes, mapping reads to the reference and resulting in a gene count matrix. R package Seurat[11] (version 3.1.1) was used to perform unsupervised clustering. To remove low quality cells and likely multiplet captures, the cells with gene numbers less than 200, or unique molecular identifier (UMI) less than 1 000, or $\log_{10}$GenesPerUMI less than 0.7 were filtered out. Furthermore, the cells with haemoglobin genes ratio of greater than 5% or mitochondrial genes ratio of greater than 10% were excluded. DoubletFinder package (version 2.0.2) was used here to identify potential doublets.

To obtain the normalized count, library size normalization was performed with NormalizeData function in Seurat. Specifically, the global scaling normalization method LogNormalize was used to normalize the gene expression for each cell, multiplied by a scaling factor (10 000 by default), and the results were log-transformed. The most variable genes were selected using FindVariableGenes function (mean.function = FastExpMean, dispersion. function = FastLogVMR) in Seurat. To remove the batch effects in the sequencing data, the mutual nearest neighbors presented by Haghverdi[12] was performed.

Graph-based clustering of cells based on gene expression profiles was performed using the FindClusters function in Seurat. Cells were visualized using a 2D uniform manifold approximation and projection (UMAP) algorithm with the RunUMAP function. To detect cluster-specific marker genes, the clusters were compared pairwise using the Seurat 'FindAllMarkers' function (test.use = presto, logfc.threshold = 0, min.pct = 0.25). Differentially expressed genes (DEGs) were used to compare the differences between two populations, which was obtained using the FindMarkers function (test.use = presto, group.by = contrasts, min.pct = 0). P value < 0.05 and |log2foldchange| > 0.58 were set as the threshold for significantly differential expression. Hypergeometric distribution in R was used to determine whether a group of DEGs were enriched in a gene ontology or a KEGG pathway term.

2.4 Pseudotime analysis

The Monocle2 package (version 2.9.0)[13] was used to determine the development pseudotime. Monocle's importCDS function was used to convert the raw count from Seurat to CellDataSet. The differential GeneTest function of the Monocle2 package was used to identify the ordering genes (qval < 0.01) that might provide the information about the ordering of cells along a pseudotime trajectory. Using the default parameters, the reduceDimension function was used to perform dimensional reduction clustering, followed by trajectory inference through the orderCells function. Using the plot_genes_in_pseudotime function, changes of gene expression were plotted over pseudotime.

2.5 SCENIC analysis

Single-cell regulatory network inference and clustering (SCENIC) analysis uses the motifs database for RcisTarget and GRNboost (SCENIC[14] version 1.1.2.2, which corresponds to RcisTarget 1.2.1 and AUCell 1.4.1) with the default parameters. The RcisTarget package was used to identify transcription factor binding motifs on a gene list that were over-represented. Each regulon group activity in each cell was assessed using AUCell package. Regulon specificity score was calculated based on Jensen–Shannon divergence, a measure of similarity between two probability distributions, to evaluate the cell type specificity of each predicted regulon. Specifically, the Jensen–Shannon divergence between each vector of bivariate regulon activity overlapped with cells of a specified cell type was calculated.[15] The scFunctions package (https://github.com/FloWuenne/scFunctions/) was used to calculate the connection specificity index.

2.6 Pathway analysis

Based on gene set file downloaded from the KEGG database (https://www.kegg.jp/), gene set enrichment analysis (GSEA) was performed using GSEABase (version 1.44.0). Gene set variation analysis (GSVA)[16] was applied using the standard settings in the GSVA package (version 1.30.0) to assign pathway activity estimates to individual cells. The LIMMA package (version 3.38.3) was used to calculate the differences between pathway activities of the individual cells.

2.7 scMetabolism analysis

The scMetabolism[17] analysis was used to quantify metabolic activity at the single-cell level. Based on the conventional single-cell matrix file, scMetabolism used VISION algorithm[18] to score and obtain the activity score of metabolic pathways in each cell. Then the significant metabolic pathways were obtained through difference analysis with bimod[19] test.

2.8 Module score analysis

AddModuleScore function in Seurat was used to calculate the average expression levels of signature (M1/M2 polarization, pro-/anti-inflammatory ability, inflammatory response, angiogenesis) on single-cell level. All the features analysed were binned based on averaged expression, and the control features were randomly selected from each bin. Gene sets used are listed in Supplementary material online, *Table S2*.

2.9 Correlation analysis between IA and distinctive control arteries

To compare the correlation between IA with different control samples, we integrated our ECs and the online Art1-3 clusters in human brain ECs (Cell Browser dataset IA: adult-brain-vasc), and employed mutual nearest neighbours to mitigate the batch effect between samples. To visualize the dataset, we used UMAP dimensionality reduction algorithms. Pearson's correlation co-efficient between IA ECs and STA/cortex artery (CA) ECs was calculated using 'cor.test' function in R.

2.10 CellChat analysis

A CellChat[20] (version 1.1.3) R package was used for the analysis of cell communication. First, the normalized expression matrix was imported to create the cellchat object with the createCellChat function. Secondly, the data was preprocessed with the identifyOverExpressedGenes, identifyOverExpressedInteractions and projectData function using the default parameters. Then, the potential ligands-receptor interactions were evaluated using the computeCommunProb, filterCommunication (min.cells = 10) and computeCommunProbPathway functions. Finally, the cell communication network was aggregated using the aggregateNet function.

2.11 Hematoxylin and eosin staining of human vascular tissues

After resection, fresh human vascular specimens were fixed in 10% formalin and then embedded in paraffin. For conventional histopathological evaluation, paraffin-embedded tissues were cut as 5 μm section. Then the mounted sections were stained with hematoxylin and eosin.

2.12 Immunofluorescence staining of human vascular tissues

Immunofluorescence staining were performed as described previously.[21] In brief, fresh samples were fixed in ice-cold 4% paraformaldehyde and sectioned while frozen. Then the sections were incubated at 4°C overnight with anti-CD31 (Abcam, UK), anti-ANGPT2 (Boster, USA), and anti-APLN (Proteintech, USA) (1:100 dilution). Primary antibodies were then visualized with species-appropriate secondary antibodies. The sections were mounted by ProLong Gold Antifade reagent with DAPI (4′,6-diamidino-2-phenylindole) (Cell Signaling Technology, USA). Then the samples were imaged under a confocal microscope.

2.13 Animal husbandry

Zebrafish (Danio rerio) husbandry were performed under standard laboratory conditions at 28°C in an automatic fish housing system (ESEN, Beijing) in 10% Hank's solution. All the experimental protocols used in this study were approved by the Institutional Animal Care and Use Committee of Institute of Neuroscience, Chinese Academy of Sciences (Protocol number NA-046-2019, renewed version NA-046-2023), and conform to the guidelines from Directive 2010/63/EU of the European Parliament on the protection of animals used for scientific purposes or the Guide for the Care and Use of Laboratory Animals published by the US National Institute of Health (NIH Publication No.85-23, revised 1996). All zebrafish transgenic lines were maintained on the Casper background. The *Tg(fli1a:DsRedEx)* line[22] was used for labelling blood vessels; the heterogeneous *Ki(pdgfrb:GAL4-VP16)* line was used for labelling mural cells together with *Tg(4 × nrUAS:GFP)*.[23] The knockdown, expression of genes and corresponding *in vivo* imaging were carried out in F0 in this work. Zebrafish embryos were euthanized by immersion in 1.5 mM of tricaine (Sigma–Aldrich, USA).[24]

The *Ki(pdgfrb:GAL4-VP16)* line was generated utilizing the CRISPR/CRISPR-associated protein 9 (Cas9) system, which we had reported in a recently published work.[25] In brief, the design of a donor plasmid involved the substitution of the left and right arms of the th-P2A-Gal4 donor plasmid with the corresponding arms derived from *pdgfrb*. The homogenous *Ki(pdgfrb:GAL4-VP16);Tg(4 × nrUAS:GFP)* line displayed defected mural cell coverage in the brain due to the mutation of pdgfrb, which in turn caused progressive abnormality of cerebrovascular morphology and emergence of the phenotypes of IA.

2.14 sgRNA design and knockdown efficiency test

To knockdown genes of interest, clustered regularly interspaced short palindromic repeats (CRISPR)/Cas9 system was used to induce zebrafish crispant. Candidate sgRNA target sites and off-target possibility were predicted using the online web site (http://CRISPR.mit.edu). Two chosen sgRNA targets for each gene were listed (Supplementary material online, *Table S3*) and synthesized (Genscript, USA). To test the efficiency of knockdown, 600 pg Cas9 protein and 125 pg of each sgRNA was injected into the one-cell stage zebrafish embryos. Then the gene knockdown efficiency in F0 embryos was examined by linking the target PCR product to pMD19-T vector (Takara, Japan) and sequenced (Supplementary material online, *Table S3*). The primer sequences are listed (Supplementary material online, *Table S4*).

2.15 *In vivo* validation in zebrafish

To specifically express the genes of interest in zebrafish ECs, the cDNAs were synthesized and cloned into the Tol2-kdrl-tetoff-H2B-mNeongreen-P2A vector (Azenta, USA), and all plasmids were verified by gene sequencing. Tol2 mRNA (20 pg) and 20 pg plasmids was injection into the one-cell stage of *Tg(fli1a:DsRedEx)* embryos, and larvae were raised and examined following the same protocol. To knockdown the genes of interest, the one-cell stage of IA zebrafish embryos was injected with Cas9 protein and sgRNAs. The injected larvae were normally raised, and the cerebrovascular pattern was examined by *in vivo* imaging at 25 days post-fertilization (dpf), and the frequency of arterial dilation and average arterial diameter were measured, to evaluate the effects of rescue.

2.16 Rescue of brain pericyte loss in the IA zebrafish

To specifically express *pdgfrb* or *pdgfrb-P2A* in the pericyte, we used the uas-Gal4 system. We cloned the full coding sequence of *pdgfrb* with or without a *P2A* sequence into a *5xuas-hsp:tdTomato* backbone vector, generating the plasmids of *5xua-hsp:tdTomato-P2A-pdgfrb* and *5xua-hsp:tdTomato-P2A-pdgfrb-P2A*. Tol2 mRNA (5 pg) and 20 pg plasmids were co-injected into the one-cell stage zygotes from the incrossed *Ki(pdgfrb:GAL4-VP16);Tg(4 × nrUAS:GFP); Tg(fli1a:DsRedEx)* adults.

2.17 Optical imaging for zebrafish brain artery

Fluorescent images were taken at room temperature using an Olympus FV3000 confocal microscope (Olympus, Japan) and processed using the software ImageJ. Live larvae or juveniles were mounted in 1% low-melting agarose (Lonza, Switzerland) containing 0.2% tricaine in 35 mm glass bottom petri dishes (MatTek, USA). The z-step of images ranged from 3 to 5 μm. The resolution of all the images was either 1 024 × 1 024 pixels or 512 × 512 pixels. For 1.5, 3.5 and 6 M brain artery imaging, we used optimized CUBIC as previous report.[26,27] The brains were fixed with 4% PFA for 24 h and then washed with cold PBS for 12 h. CUBICR1 treatment was then performed at 37°C for 24 h.

2.18 Statistics

No statistical methods were used to predetermine sample size. Animals were assigned to experimental groups using simple randomization, without investigator blinding. For animal experiments, the significance of difference between two groups was determined by using unpaired two-tailed Student's *t*-test. Calculations were performed by using GraphPad Prism v9.0 software. Data were represented as mean ± SEM in all figures. **** indicates $P < 0.0001$, ns indicates $P > 0.05$.

3. Results

3.1 Overall cell populations in IA and the control arterial wall

To profile cellular and molecular signatures of human IA tissues, we obtained IA and the STAs from donors undergoing craniotomy (*Figure 1A*). The samples were dissected and digested by the established methods. Dissociated cells from six individuals (three controls and three IAs) were processed for scRNA-seq using the 10× Genomics Chromium platform (*Figure 1A*). After quality control and filtering (Supplementary material online, *Figure S1A–E*), whole cell transcriptomes with high-quality from 43 462 cells were obtained.

Nine major cell populations were identified, and each cluster displays a unique set of enriched genes (*Figure 1B–D* and Supplementary material online, *Table S5*). In brief, the nine major cell types included three vascular cell populations (ECs, vSMCs and perivascular fibroblasts), five types of immune cells (T/NK cells, B cells, myeloid cells, mast cells, neutrophils) and oligodendrocytes (*Figure 1B*). Compared with the control artery, IA showed significantly enriched proportions of most immune cells and

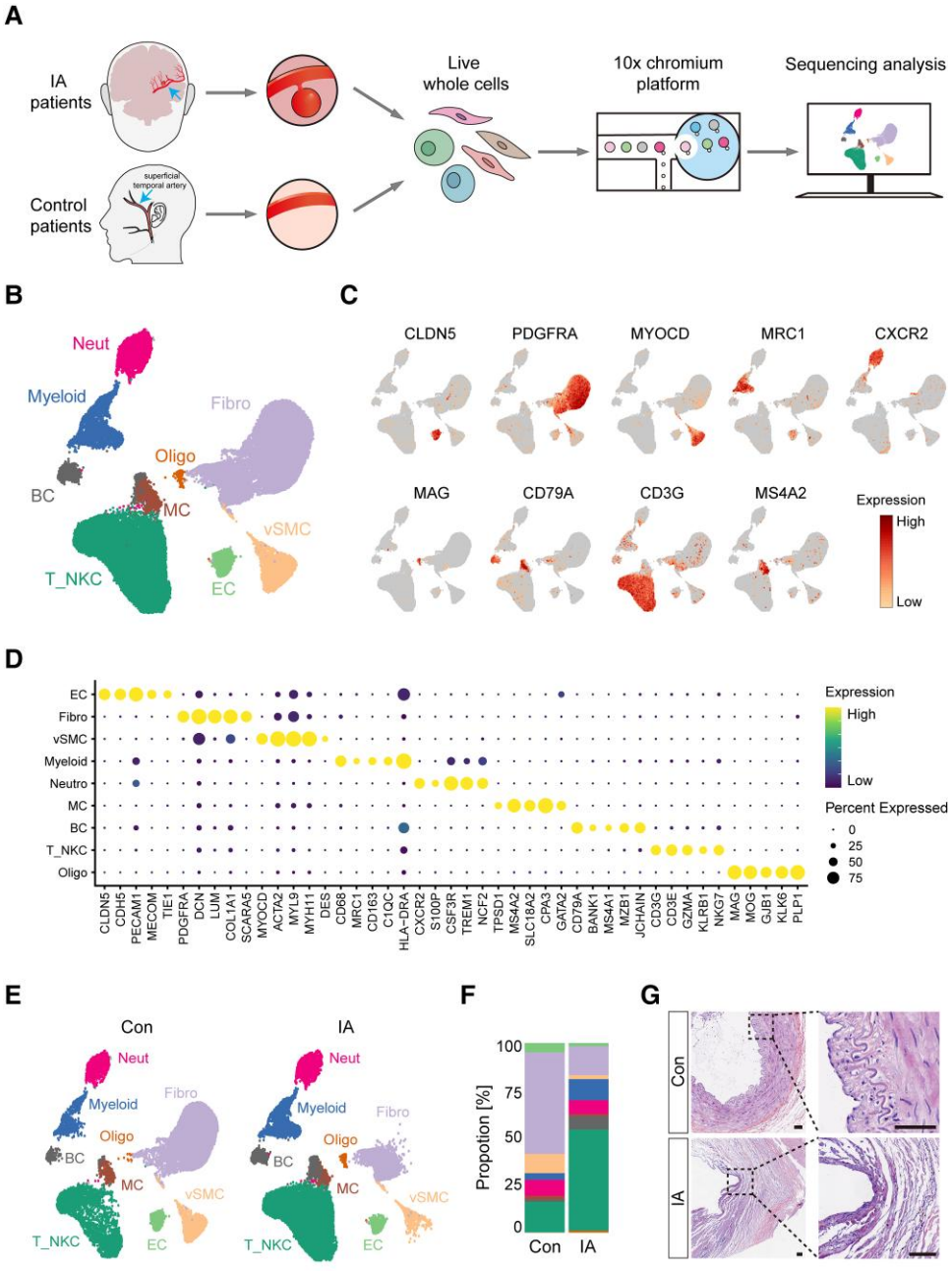

Figure 1 scRNA-seq profiling of human IA and control STA. (*A*) Schematic representation of sample collection, single cell preparation, sequencing, and bioinformatic analysis. (*B*) UMAP plot showing nine cell clusters for all cells in IA and STA. (*C*) UMAP plot showing the expression of selected marker genes in the defined cell types in (*B*). (*D*) Dot plot showing the expression of selected marker genes in the defined cell types in (*B*). (*E*) UMAP plot showing distinct distribution of nine cell clusters in IA and STA. (*F*) Bar graph showing distinct proportions of nine cell clusters in IA and STA. (*G*) HE staining showing vascular morphology of STA (upper) and IA (down) tissue. BC, B cell; T_NKC, T and Natural killer cell; EC, endothelial cell; Fibro, fibroblast; Myeloid, myeloid cell; MC, mast cell; Neut, neutrophil; vSMC, vascular smooth muscle cell; Oligo, oligodendrocyte. Scale bar: 50 μm.

reduced proportions of the vascular cells (*Figure 1E* and *F* and Supplementary material online, *Table S6*), which is consistent with the current understanding of the disease.[4] The HE staining also validated the pathologic vascular morphology in IA (*Figure 1G*).

3.2 Endothelial aberrancy in IA patients

ECs line the inner and the blood-facing surface of cerebral arteries, and the pathologic changes of ECs have been suggested to be the earliest step in IA formation.[28] Further unsupervised clustering of ECs gave rise to four EC subclusters (EC1–EC4) (*Figure 2A*). With an integral loss of ECs, the EC4 was specifically enriched, while the EC1, EC2, and EC3 were significantly decreased in IA (*Figure 2A* and *B* and Supplementary material online, *Figure S2A and Table S6*). Based on DEGs, marker genes and metascape[29] GO enrichment analysis, we obtained insights in the putative biological role of each EC cluster. The GO terms 'response to cell death' and 'cellular response to cytokine' were enriched in EC1 (Supplementary material online, *Figure S2B*). Except an elevated level of *SEMA3E*, several cytokines,

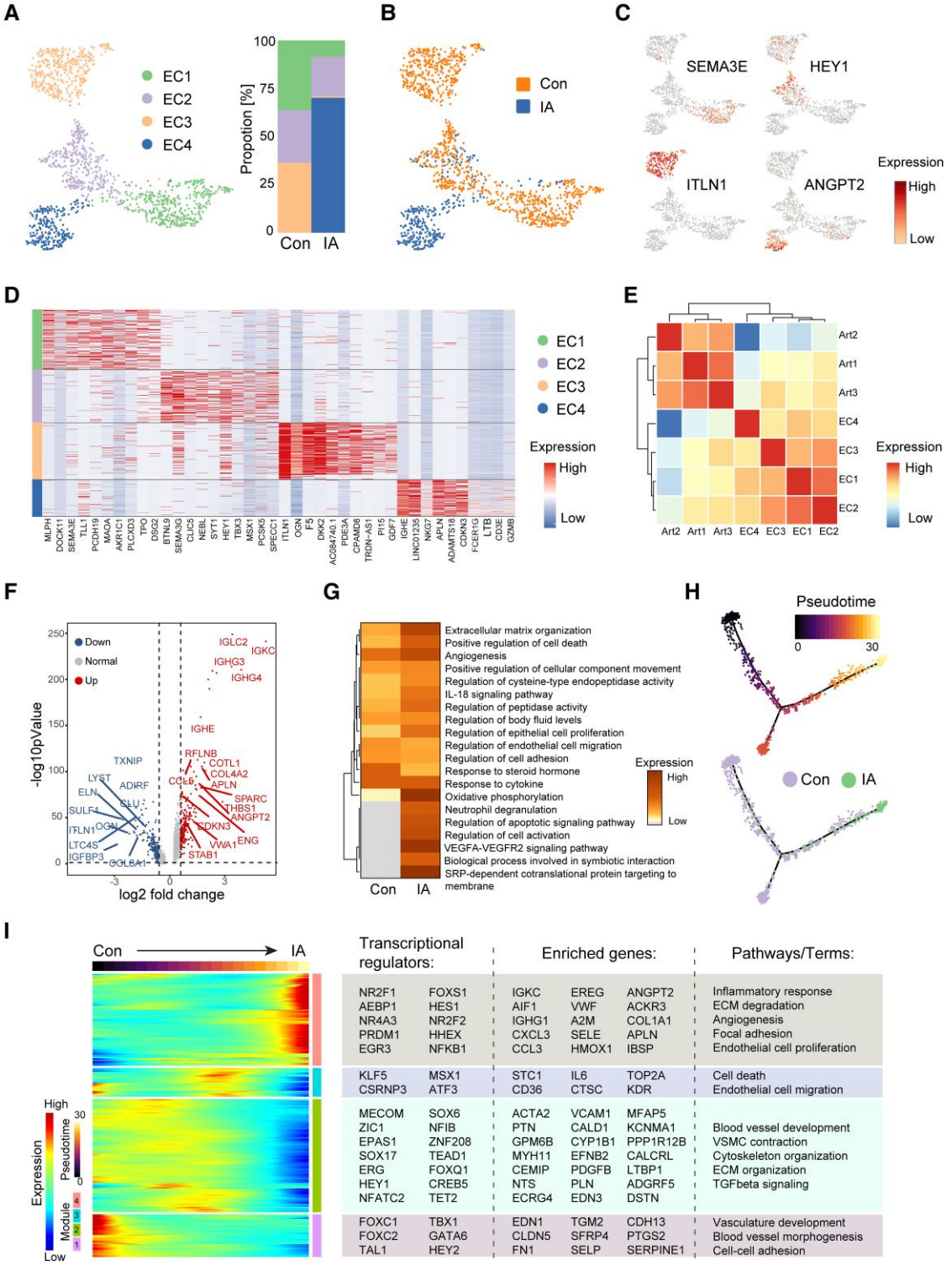

Figure 2 Endothelial aberrancy in IA patients. (*A*) Subclustering of ECs. Left, UMAP plot showing four subclusters of ECs in IA and STA; right, bar graph showing distinct proportions of the defined EC subclusters. (*B*) UMAP plot showing distinct clustering distribution of IA and STA derived ECs. (*C*) UMAP plot showing the expression of selected marker genes in the defined EC subclusters in (*A*). (*D*) Heatmap showing top DEGs in the defined EC subclusters in (*A*). (*E*) Heatmap showing average correlation scores between EC subcluster Art1–Art3 (CA derived) and subcluster EC1–EC4 (IA and STA derived). (*F*) Volcano plot showing DEGs between IA and STA derived ECs. (*G*) Heatmap showing enriched pathways in IA and STA derived ECs, by metascape analysis. (*H*) Pseudotime analysis of IA and STA derived ECs, by monocle. (*I*) Dynamic molecular changes along the pseudotime analysis. Left, heatmap showing gene expression pattern of each module; right, lists of significantly enriched transcription factors, genes, and pathways along the pseudotime trajectory. EC, endothelial cell; CA, cortex artery.

immune receptors and adhesion molecules, such as *CCL14*, *ACKR1*, *IL6*, *SELE*, *IL1R1*, *LIFR* were highly expressed in EC1 (*Figure 2C* and *D* and Supplementary material online, *Table S7*). The cluster EC2 enriched for 'blood vessel development' and genes important for EC migration and Notch regulation (*HEY1*, *SEMA3G*) (*Figure 2C* and *D* and Supplementary material online, *Figure S2B*). The EC3 represented a high level of 'circulatory system process', and enriched for *ITLN1*, which supported the positive regulation of glucose import (*Figure 2C* and *D* and Supplementary material online, *Figure S2B*). The EC4 expressed genes involved in 'VEGFA-VEGFR2 signaling pathway' and 'extracellular matrix organization' (*Figure 2C* and *D* and Supplementary material online, *Figure S2B*). Further SCENIC analysis revealed that regulons FOSL2, HES1, and RUNX3 were highly activated in EC4, supporting its functions in cell proliferation, differentiation, transformation, and angiogenesis (Supplementary material online, *Figure S2C*).[30–37] Using a previously annotated human cerebral cortex vasculature,[38] we showed a higher Pearson correlation coefficient between our control STA and IA ECs (EC1–EC4) compared to the cortex artery (CA) derived ECs (Art1–Art3) (*Figure 2E* and Supplementary material online, *Figure S2D and E*). The significant differences lining between STA and CAs included 'regulation of blood circulation' and 'muscle relaxation' by performing DEGs and GSEA (Supplementary material online, *Figure S2F and G*). Compared with the control, ECs in IA showed great differential gene expression, especially with the up-regulated *ANGPT2* and *APLN*, both of which were markers of tip cells and involved in angiogenesis (*Figure 2F*).[39–41] The same significant expression of *ANGPT2* and *APLN* also came from the comparison between IA and CA derived ECs (Supplementary material online, *Figure S2H*). Besides, the immunofluorescence staining further confirmed the expression of both markers in human IA lesion (Supplementary material online, *Figure S2I*). And metascape analysis confirmed that several pathogenic cascades, such as ECM organization, inflammation, apoptosis, angiogenesis, and oxidative phosphorylation, were significantly up-regulated in IA (*Figure 2G*). In addition, the SCENIC and scMetabolism analysis also suggested a largely alternant regulon activity and metabolic status in the ECs of IA (Supplementary material online, *Figure S2J and K*).

Pseudotime analysis of ECs revealed a consensus molecular trajectory from control to IA (*Figure 2H* and Supplementary material online, *Figure S2L*), and it predicted a progressive up-regulation of module involved in inflammatory response and angiogenesis, and down-regulation of module involved in blood vessel morphogenesis and cell–cell adhesion/junction, marked by distinct sets of transcriptional factors, developmental genes and signaling pathways (*Figure 2I*).

3.3 Dynamic vSMCs and perivascular fibroblasts in IA

The vasculature of the cerebral artery is surrounded by vSMCs and perivascular fibroblasts. Both types of cells not only act as a supporting framework, but also play important roles for the behaviours of ECs during angiogenesis and homeostasis.[42]

The vSMCs showed a heterogeneous distribution in the clustering plot (Supplementary material online, *Figure S3A*). We obtained five clusters of vSMCs from all six samples (Supplementary material online, *Figure S3A*). Among which, vSMC4 and vSMC5 were significantly enriched while the other clusters were almost absent in IA (Supplementary material online, *Figure S3A and B*). vSMC5 highly expressed *DSP*, *CDH2*, *HMCN1*, which were major contributors to cell–cell adhesion.[43–45] By contrast, vSMC4 was characterized by *CHST2*, majoring in adhesion and migration of leucocytes to ECs,[46] and *PLXDC1*, *GPR4*, both of which had been reported to regulate angiogenesis (Supplementary material online, *Figure S3C and D*).[47,48] In the control artery, vSMC1 enriched for cell cycle regulation genes *KLF4*, *ATF3* and *JUN*, together with GO pathway 'vasculature development', while vSMC2 represented the most contractile phenotype (Supplementary material online, *Figure S3E and Table S8*). vSMCs normally display a contractile phenotype for regulating the diameter of arteries and neurovascular coupling.[49] Here, our data showed an obvious reduction of known contractile markers (*MYH11*, *CNN1*, *DES*) and increased expression of inflammation related genes (*VCAM1*, *HLA-A*, *FN1*) in vSMC of IA, suggesting a phenotypic switching (Supplementary material online, *Figure S3F*). Further DEG analysis showed that vSMCs of IA were enriched for the transcripts of *VCAN*, *POSTN*, *SULF1* and *SPARC* (Supplementary material online, *Figure S3G*), which were implicated in modulating the growth and migration of vSMCs through ECM remodeling or TGF-β signaling pathway.[50–53] The decreased expression of *CLU*, *ADAMTS1*, and *KCNMA1* was also indicative of the dysregulated phenotype in IA vSMC (Supplementary material online, *Figure S3G*). Inflammatory vSMC-mediated EC dysfunction has been extensively explored.[54] GSVA showed that vSMCs in IA were characterized by the up-regulated EC adhesion and sprouting angiogenesis signaling (Supplementary material online, *Figure S3H*). And the dysregulated ion modulation pathway of calcium, potassium, chloride, together with the SMC relaxation suggested a neurovascular uncoupling (Supplementary material online, *Figure S3H*).

By using the annotations from previous human and mouse studies, we identified a total of seven distinct subtypes of perivascular fibroblasts (Supplementary material online, *Figure S4A*). Among which, proportions of clusters 4, 6, and 7 were enriched in IA (Supplementary material online, *Figure S4A and B*). *POSTN* and *TGM2*, known for their roles in the induction of arterial calcification,[55,56] were significantly enhanced in fibroblast clusters 4 and 6 (Supplementary material online, *Figure S4C and Table S9*). While clusters 2 and 3 showed higher expression of microfibrillar-associated protein encoding genes *MFAP4* and *MFAP5* (Supplementary material online, *Table S9*), which had been reported to associate with thoracic and abdominal aortic aneurysm through the regulation of ECM and SMCs proliferation.[57–59] The DEGs analysis also indicated an elevated expression of heparin-binding cytokine *PTN* in IA, which involved in pathological angiogenesis.[60] Whereas *CNN5*, a regulator for the generation of SMCs, and *MYOC*, which encodes the protein myocilin, were significantly down-regulated in IA fibroblasts (Supplementary material online, *Figure S4D*). The metascape GO analysis revealed substantially differential properties in fibroblasts of IA, such as decreased proliferation and growth, lowered response to hormone and growth factors, increased ossification, cell adhesion and integrin 1 pathways (Supplementary material online, *Figure S4E*). Furthermore, the SCENIC analysis revealed higher specificity of STAT1, ETV7, and CREM regulons in the IA fibroblasts, whereas the regulons JDP2, ARID5B and ATF4 were more specific in the control artery (Supplementary material online, *Figure S4F*).

3.4 Heterogeneity of immune cells in IA

Myeloid cells were significantly enriched in IA (*Figure 1E* and *F* and Supplementary material online, *Table S6*). Re-clustering of the myeloid cells revealed four clusters, including three clusters of macrophages (Mϕ1–Mϕ3) and one cluster of DC (Supplementary material online, *Figure S5A and B*). Macrophage has been well documented for its implications in the formation and rupture of IA in humans.[61,62] Different subpopulations of macrophages orchestrate the innate immune activities.[63] Mϕ1 cells displayed higher expression of *FCN1* and *S100A12*, indicating their potent inflammatory activities (Supplementary material online, *Figure S5C*). The Mϕ2 cluster was characterized by *C1QC*, *FOLR2*, and *LYVE1* expression (Supplementary material online, *Figure S5C*), which served as the most conserved macrophage.[63] The cluster Mϕ3 increased significantly in IA group (Supplementary material online, *Figure S5A*). According to the known marker genes *FCGR3A* for M1 and *CD163* for M2, we speculated the Mϕ3 as a M1-like macrophage subcluster (Supplementary material online, *Figure S5D*). Further AddModuleScore analysis of M1/M2-like polarization and pro-/anti-inflammatory scores based on marked gene sets (Supplementary material online, *Table S2*) supported that conclusion (Supplementary material online, *Figure S5E*). In addition, we observed increased expression of *SPP1* in the Mϕ3 (Supplementary material online, *Figure S5D*). SPP1, known as osteopontin, has been found to be associated with abdominal aortic aneurysm formation through its roles in leucocyte recruitment.[64] The DC cluster accounted for a relatively small portion of myeloid cells and showed less heterogeneous distribution

(Supplementary material online, *Figure S5A and B*). And the enriched expression of *CD1C*, *FLT3*, and *FCER1A* in DCs indicated their potent antigen-presenting ability (Supplementary material online, *Figure S5C*).

Similarly, there were more lymphocytes infiltrated into IA compared with the control (*Figure 1E* and *F* and Supplementary material online, *Table S6*). T cells were the most abundant cell population, comprising 79.9% and 85.4% of infiltrating lymphocytes in control and IA tissues, respectively (Supplementary material online, *Figure S5H*). While B cells and NK cells were comparatively less in number (Supplementary material online, *Figure S5H*), which was consistent with the previous study.[65] The re-clustering of T cells revealed 10 subclusters, including five CD4+ T cells subtypes and five subclusters of CD8+ T cells (Supplementary material online, *Figure S5F*). CXCR3+ CD4 cells were enriched in IA tissue and were served as effector-like cells based on high expression of cytotoxic cytokines (*GNLY*, *GZMA*, *GZMB*, *GZMK*, *IFGN*, *NKG7*) and exhaustion-related transcription factors (*EOMES*, *TOX*, *HOPX*, *ZNF683*, *ZEB2*).[66] Whereas the GZMA + CD4 cells moderately expressed such genes (Supplementary material online, *Figure S5F–I*). In contrast, memory-like NR4A1+ CD4 cells (with high expression of *CD69*, *RUNX3*, and *NR4A1*)[67] and naive CCR7+ CD4 cells (with high expression of *CCR7*, *TCF7*, *LEF1*, and *SELL*) were decreased in IA (Supplementary material online, *Figure S5F–I*). And the FOXP3+ CD4T cells highly expressed regulatory genes of *IL2RA*, *FOXP3*, and *IKZF2* (Supplementary material online, *Figure S5G*), same as the previously reported.[68] The GZMK+ and GZMB+ CD8 cells, which were defined as cytotoxic T cells represented larger proportions of CD8T cells in IA (Supplementary material online, *Figure S5H and I*). More CD28+ CD8 cells infiltrated into IA, which displayed elevated expression of co-stimulatory and exhausted molecules *CTLA4*, *CD28*, *PDCD1* (Supplementary material online, *Figure S5F–I*). The proportion of resident memory-like NR4A1+ CD8 cells increased from 2.83% to 17.65% in IA compared with the control, while the naive CCR7+ CD8 cells showed no significant differences (Supplementary material online, *Figure S5H and I*).

3.5 Abnormal cellular communication in IA

Cell–cell communications play important roles in maintaining tissue homeostasis. How aberrant cell communications implicate in the pathological dilation of cerebral arteries remains unclear. To explore the complex interactions among different cell types, we inferred all potential intercellular communications by analysing the expression of ligand–receptor pairs using CellChat analysis. Compared to the control artery, there were significantly increased number and strength of cell–cell interaction in IA (*Figure 3A–D* and Supplementary material online, *Figure S6A–D*). While the alteration of connections between vascular cells ranked the top, marked changes between immune cells and vascular cells were also observed in IA (*Figure 3A–D* and Supplementary material online, *Figure S6A–D*).

Specifically, we found several altered outgoing and incoming signaling pathways related to angiogenesis, such as VEGF, ANGPT, APLN, SEMA4, CCL, and CXCL signaling (Supplementary material online, *Figure S6E–J*). Previous study revealed that ANGPT2 destabilized blood vessels by antagonizing the signaling of ANGPT1 to TIE2.[69] ANGPT2 signaling was undetected in the control, but it significantly increased between IA ECs (*Figure 3E* and *F*). The abnormal upregulation of ANGPT2 in ECs was also observed in a recent finding in the mouse brain vasculature.[39] As we mentioned above, APLN was enriched in tip cells and suggested to promote vascular outgrowth and EC proliferation.[40] Similarly, the APLN-APLNR signalling anomalously appeared in the IA ECs (*Figure 3E* and *F*). The chemokine signalling axis CXCL12-ACKR3/CXCR4, which supported the physiological process such as EC migration and arterial morphogenesis,[70–72] was found elevated between EC and perivascular cells in IA (*Figure 3E* and *F*). Besides, we found SEMA4A signalling, a negative regulator of embryonic vascularization and VEGF-mediated angiogenesis,[73] was downregulated in IA (*Figure 3E* and *F*). Inflammation response, critical for IA pathogenesis,[28] also showed significant alterations. For instance, the ITGB2-ICAM1 signalling pair was enriched between immune cells and ECs and fibroblasts in IA (*Figure 3E* and *F*), which had been implicated in leucocyte adhesion and transmigration.[74,75] While another signalling pair ADGRE5-CD55 sharing the similar function was less activated (*Figure 3E* and *F*).

These data consistently revealed the significant increase of both inflammation and angiogenesis in IA. To further explore the relationship lines between inflammation and angiogenesis, we performed AddModuleScore analysis based on marked gene sets (Supplementary material online, *Table S2*). The results showed that each sample displayed a distinct inflammatory and angiogenic status (Supplementary material online, *Figure S7*), which could be further used to interpret the disease progression. As the angiogenic score of ECs correlated loosely with the inflammatory score of ECs ($R = 0.59$) (Supplementary material online, *Figure S7A*), we re-analysed that with the inflammatory levels of immune cells (myeloid cells, T/NK cells). Surprisingly, while T/NK cells showed similar correlation to that of the inflammatory score of ECs ($R = 0.57$), the inflammatory response of myeloid cells correlated more with the angiogenic score of ECs ($R = 0.99$) (Supplementary material online, *Figure S7B and C*), suggesting the mutually reinforcing effects between the inflammatory response of myeloid cells and the angiogenesis of ECs.

3.6 Ectopic *angpt2a* expression causes vascular abnormality

To further validate these significantly altered signaling pathways/genes *in vivo*, we specifically expressed *angpt2a*, *apln*, *cxcl12b*, *cxcr4a*, or *ackr3a* in the ECs of zebrafish, via the injection of plasmids with the EC-specific *kdrl* promoter and the corresponding cDNAs (*Figure 4A*). The transient injection of plasmids into the fertilized eggs of EC-labelling transgenic line *Tg(fli1:DsRed)* enables the mosaic labelling of ECs so that we can compare the morphology between the mNeonGreen + DsRed + ECs (with the expression of corresponding cDNAs) and mNeonGreen- DsRed + ECs (the control ECs without the expression) (*Figure 4A*). After injection of the *flk1:angpt2a* plasmid, we compared the patchily labelled cerebral vessels (with mNeonGreen + DsRed + ECs) to their corresponding locations of vessels (with mNeonGreen- DsRed + ECs). We found the mosaic *angpt2a* expression in zebrafish ECs significantly increased the vascular diameters in the brain (*Figure 4B* and *C* and Supplementary material online, *Figure S8A*). In addition, we observed more ECs assembled in the vessels, which present an irregular arrangement as well (*Figure 4B* and *D* and Supplementary material online, *Figure S8A*). However, the cerebral vessels with EC-specific expression of *apln*, *cxcr4a*, *ackr3a*, *or cxcl12b* in the *Tg(fli1a:DsRed)* showed no obvious morphological differences between the vessels with the mNeonGreen + DsRed + and the mNeonGreen- DsRed + ECs (*Figure 4C* and *D* and Supplementary material online, *Figure S8B*). These data highlight an intriguing role of *angpt2a* in promoting the dilation of ECs during IA.

3.7 An innovative IA model and *in vivo* rescue of IA in zebrafish

To further test the identified IA-related genes from the patients, we do need a genetic animal model for IA. Although there have been reported IA animal models made by using elastase in combination with other drugs or surgical procedures,[76] a genetic IA animal model with consistent IA phenotypes suitable for continuous *in vivo* tracking has yet to be established. Previous reports had shown that the loss of vSMCs, the predominant cell type within the aortic wall, directly related to IA development and progression.[77–80] Thus, here we determined to make a genetically modified vertebrate model that mimics the IA-like phenotypes by targeted vSMC loss.

Platelet-derived growth factor (PDGF) signalling plays critical roles in mural cell development, such as the recruitment and expansion of the mural cell progenitors, therefore its aberrance resulting in the decreased coverage of mural cells on blood vessels.[81–83] Here, we strikingly found differential cell communication interactions of PDGF signalling pathways between IA and STA cells, mainly exhibiting an emerging interaction between vSMCs, fibroblasts, and macrophages appeared in the IA tissues

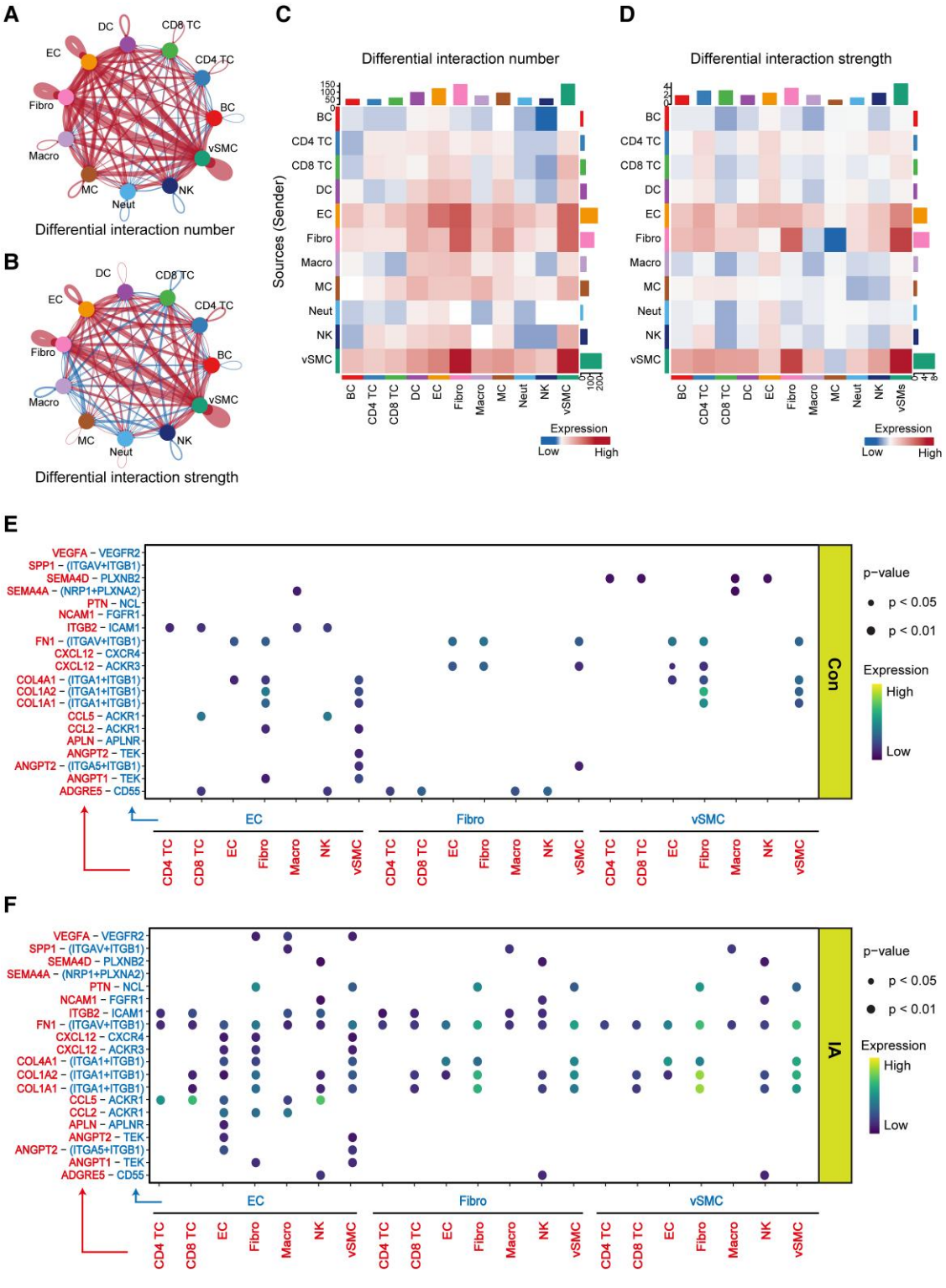

Figure 3 Cell–cell communications in IA patients. (*A*, *B*) Circle plot showing differential interaction number (*A*) and strength (*B*) between IA and STA cells. (*C*, *D*) Heatmap showing the differential interaction number (*C*) and strength (*D*) between IA and STA cells. (*E*, *F*) Dot plots showing the indicated ligand–receptor communication intensity among STA (*E*) and IA (*F*) cells. BC, B cell; TC, T cell; DC, dendritic cell; EC, endothelial cell; Fibro, fibroblast; Macro, macrophage; MC, mast cell; Neut, neutrophil; NK, natural killer cell; vSMC, vascular smooth muscle cell.

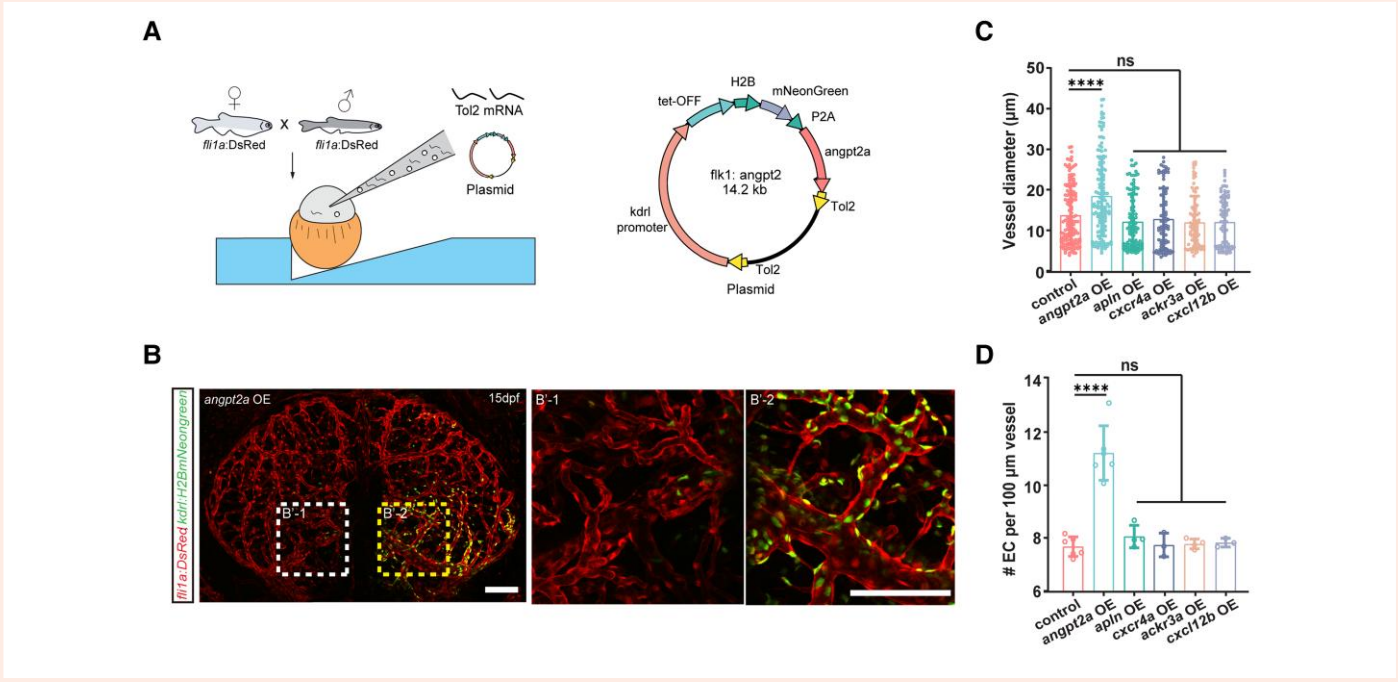

Figure 4 Mosaic *angpt2a* expression causes vascular abnormality. (*A*) Left, schematic representation of EC-specific expression of *angpt2a* in zebrafish; right, schematic of the injected plasmid. (*B*) Confocal imaging of cerebral vessels with mosaic *angpt2a* expression in 15 dpf fish. Left, cerebral vessels with patchy *angpt2a* expression; right, zoomed typical cases in left. (*C*) Bar graph showing diameters of vessels with mosaic over-expression and the control vessels in 15 dpf fish. $n = 6$ for control and *angpt2a* OE fish, $n = 3$ for *apln*, *cxcr4a* or *cxcl12b* OE fish, and $n = 4$ for *ackr3a* OE fish. Student's unpaired *t*-test, mean ± SEM, $^{****}P < 0.0001$. (*D*) Bar graph showing EC density of vessels with mosaic over-expression and control vessels in 15 dpf fish. $n = 6$ for control and *angpt2a* OE fish, $n = 3$ for *apln*, *cxcr4a* or *cxcl12b* OE fish, and $n = 4$ for *ackr3a* OE fish. Student's unpaired *t*-test, mean ± SEM, $^{****}P < 0.0001$. OE, over-expression. Scale bar: 100 μm.

(Supplementary material online, *Figure S9A*). Among the pathway, PDGF receptor beta is a typical receptor tyrosine kinase encoded by the *PDGFRB* gene, which had been reported to implicate in IA.[84] Also here we presented the expression level of it within distinctive cell subtypes (Supplementary material online, *Figure S9B*).

Through targeting *pdgfrb* with an established method,[85] we generated a knockin line *Ki(pdgfrb:GAL4-VP16);Tg(4 × nrUAS:GFP)*, for the labelling of the mural cells, including pericytes and SMCs (*Figure 5A*). As we had reported the heterozygous *Ki(pdgfrb:GAL4-VP16);Tg(4 × nrUAS:GFP)* (referred as *pdgfrb*$^{Ki/+}$) showed robust and specific mural cell labelling,[25] whereas we further found the homozygous *Ki(pdgfrb:GAL4-VP16);Tg(4 × nrUAS:GFP)* (referred as *pdgfrb*$^{Ki/Ki}$) exhibited complete loss of brain pericytes (*Figure 5A* and Supplementary material online, *Figure S9C*), resembling the phenotype of loss-of-pericytes in the PDGFB-PDGFRB signaling mutant.[83,86–88] As our intron targeted knockin method does not destroy the integrity of the targeted gene,[85] so we wonder how the function of the gene is destroyed by the knockin. We checked the details of the *pdgfrb-P2A-Gal4* cassette and found the P2A self-cleaving peptide sequence used for bicistronic expression will lead to the fusion of its 21-amino-acid peptide to the C-terminal of Pdgfrb (*Figure 5A*).[89] Therefore, we reasoned that the P2A tag suppressed the function of PDGFRB. To test it, we transiently express the wild-type *pdgfrb* or *pdgfrb-P2A* in the mural cells of the progeny embryos of the homozygous *pdgfrb*$^{ki/ki}$ by one-cell stage injection. As we expected, transient injection of wild-type *pdgfrb* partially rescued the loss of brain pericyte phenotype of the *pdgfrb*$^{ki/ki}$, whereas the *pdgfrb-P2A* failed to rescue (Supplementary material online, *Figure S10A*). This data indicates Pdgfrb-P2A is a loss-of-function form of the wild-type Pdgfrb, which destroys the Pdgfb-Pdgfrb signalling that resulted in the brain mural cell development deficiency.[83,88]

Compared with control, *pdgfrb*$^{ki/ki}$ exhibited abnormal arterial local dilations and ballooning protrusions that accompanied by the loss-of-SMCs (*Figure 5B* and *C*). Hereafter we referred to the *pdgfrb*$^{ki/ki}$ line as IA-like zebrafish. The IA phenotypes started to appear around 15–25 dpf and persisted into adulthood (*Figure 5D*, Supplementary material online, *Figures S9D and E* and *S11A–C*), resembling the typical phenotypes of aneurysmal cerebral arteries in human patients. As the IA-like zebrafish can survive to adulthood and fertile, we can observe the IA formation and progression directly with naked eyes through the skull at various development and adult stages (see Supplementary material online, *Figure S9D and E*). And at later adult stage, the phenotype of arterial dilation got much more severe (*Figure 5E*). The frequency and the diameter of the dilated arteries displayed an age-dependent progression (see Supplementary material online, *Figure S11A–C*), resembling the time course of aneurysm development in human.[1,90] Although the diameter of the affected arteries greatly expanded, the diameter of the brain capillaries only slightly increased (see Supplementary material online, *Figure S11A–C*). Together, our IA-like zebrafish model recapitulates the key pathological features of IA in human patients, which makes it an excellent *in vivo* model for the study of the molecular and cellular mechanisms of IA.

Next, we knocked down *angpt2a*, *apln*, *cxcl12b*, *cxcr4a*, or *ackr3a* in the IA zebrafish by using the crispant method[91] (*Figure 6A*). Compared to the control injected fish, knocking down of *angpt2a* caused a significant reduction in arterial diameter in the 25 dpf IA zebrafish, while the frequency of dilated arteries showed no difference (*Figure 6B* and *C* and Supplementary material online, *Figure S12A*). Similarly, the *apln* crispant zebrafish also displayed ameliorated dilation of penetrating arteries (*Figure 6B* and *C*). However, we found the knockdown of *cxcl12b* in zebrafish causing a high embryo lethality, and the knockdown of *cxcr4a* and *ackr3a* could not alleviate the occurrence frequency nor arterial phenotypes in IA zebrafish (Supplementary material online, *Figure S12A and B*). In all, the above data suggest the potential role of *angpt2a* and *apln* in IA progression.

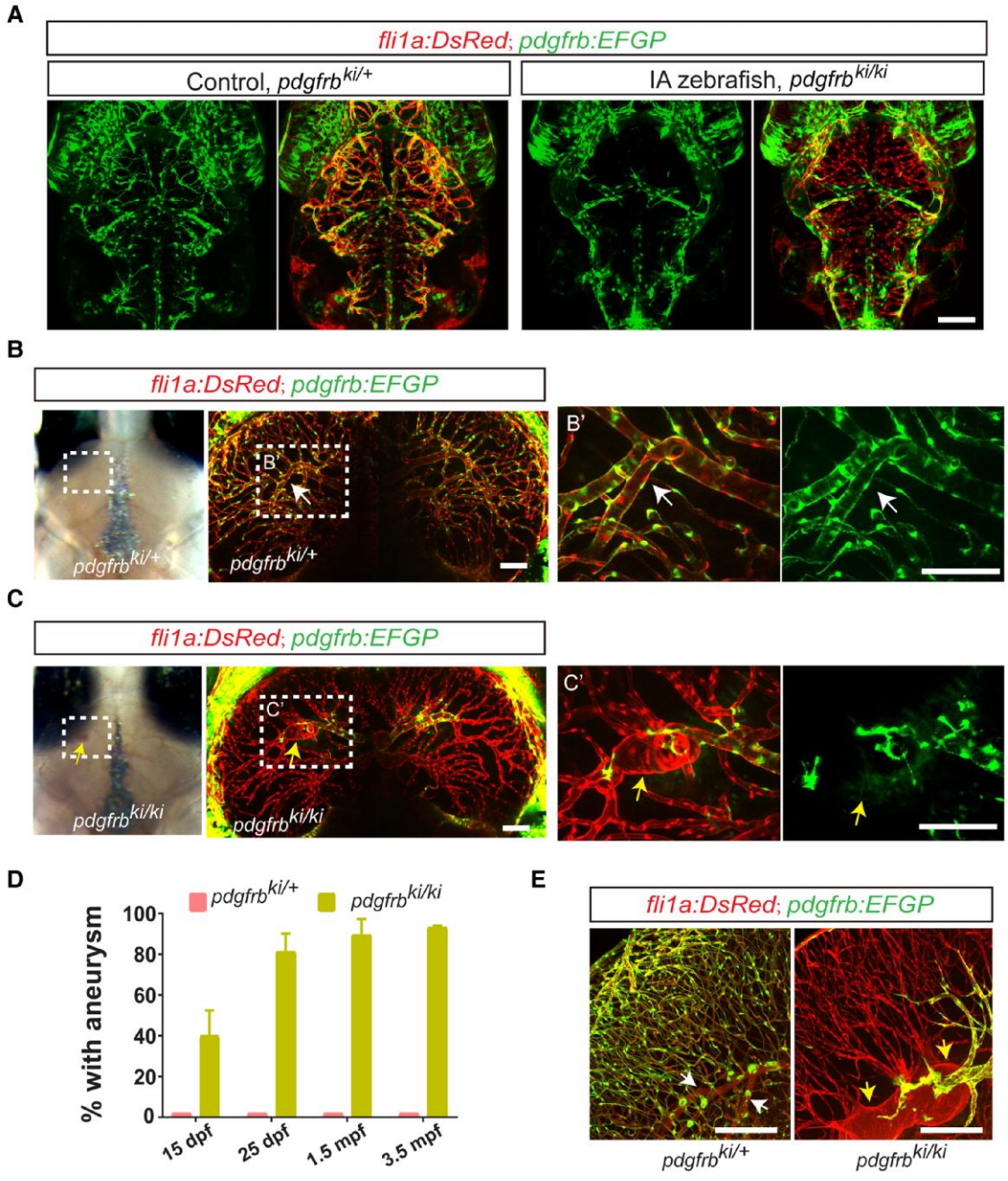

Figure 5 A novel mural cell-deficient zebrafish model develops IA-like phenotypes. (*A*) Confocal imaging of representative mural cell deficiency in 4.5 dpf control (*pdgfrb*$^{ki/+}$, left) and IA (*pdgfrb*$^{ki/ki}$, right) zebrafish. (*B*, *C*) Light field and confocal imaging of arterial dilations in 25 dpf control (*pdgfrb*$^{ki/+}$, *B*) and IA (*pdgfrb*$^{ki/ki}$, *C*) zebrafish. Right, zoomed typical phenotypes in the left. (*D*) Bar graph showing percentages of zebrafish with arterial dilations at 15, 25 dpf, 1.5 months post-fertilization (mpf) and 3.5 mpf. $n = 39$ for 15 dpf, $n = 44$ for 25 dpf, $n = 45$ for 1.5 mpf and $n = 29$ for 3.5 mpf IA (*pdgfrb*$^{ki/ki}$) zebrafish, mean ± SEM. (*E*) Confocal imaging of arterial dilations in 6.0 mpf adult control (*pdgfrb*$^{ki/+}$, left) and IA (*pdgfrb*$^{ki/ki}$, right) zebrafish. Scale bar: 100 μm.

4. Discussion

The dysfunction and damage of ECs are suggested to be the first event in human IA pathogenesis.[28,92–94] The present study provides insights into the critical genes and molecular pathways in ECs involved in IA formation. This was made possible by obtaining high-quality EC samples for scRNA-seq analysis, which has been a challenge in the past due to the extensive degeneration and loss of ECs during IA progression,[95,96] or the low efficiency of EC recovery during sample preparation.[10,38,97,98] Our results showed the presence of four distinct EC subclusters, with the EC4 subcluster being significantly enriched in IAs compared to the control samples (*Figure 2A*). The metascape enrichment analysis highlighted dysregulated activities in various functional categories such as ECM organization, EC proliferation, cell death, cell motility, and inflammation in the EC4 subcluster (Supplementary material online, *Figure S2B*). Furthermore, the pseudotime analysis revealed a trajectory from EC1–EC3 to EC4, suggesting a progressive transformation of ECs during IA formation and progression.

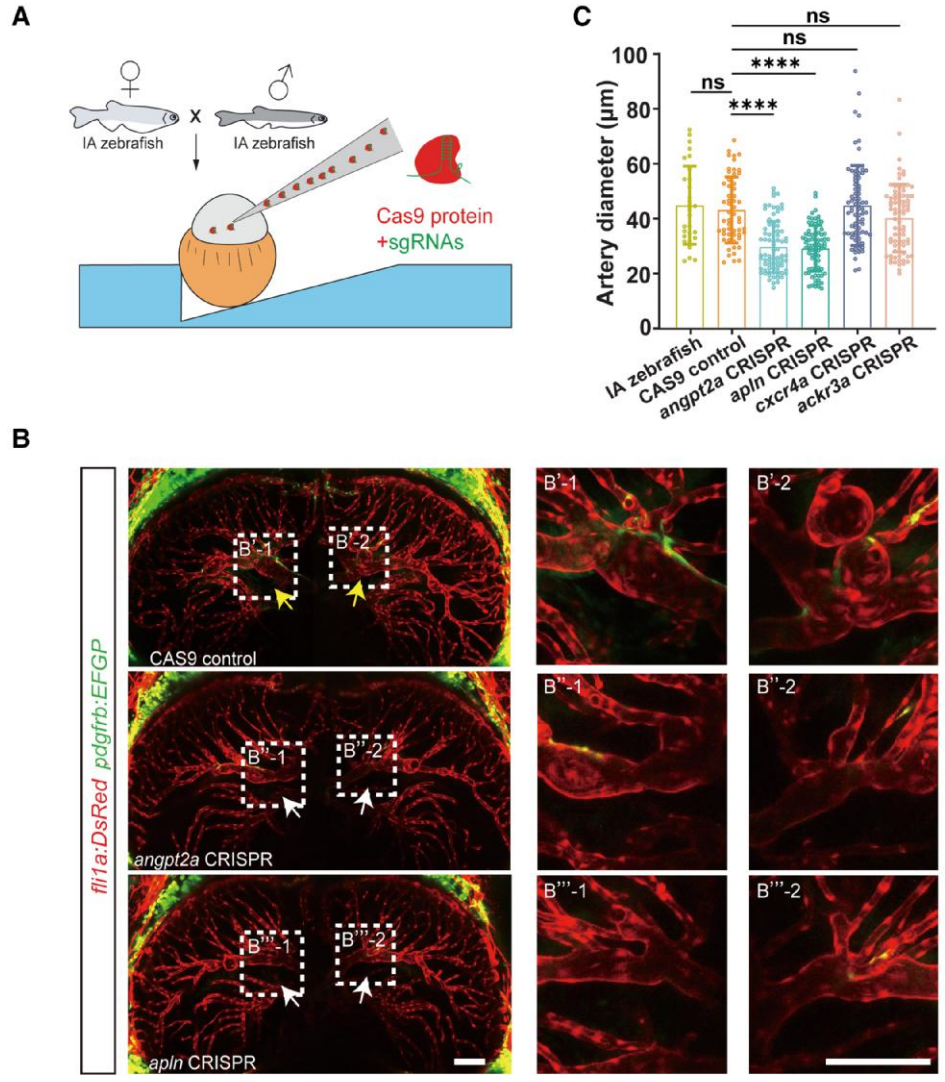

Figure 6. *In vivo* rescue of the phenotypes in IA-like zebrafish by knocking down *angpt2a*. (*A*) Schematic representation of the target gene knockdown in the IA-like zebrafish by using the crispant method. (*B*) Confocal imaging of arterial dilations in 25 dpf Cas9 control, *angpt2a* or *apln* crispant IA-like zebrafish. (*C*) Bar graph showing artery diameters in 25 dpf Cas9 control, *angpt2a*, *apln*, *cxcr4a* or *ackr3a* crispant IA-like zebrafish. $n = 5$ for each group, four penetrating arteries per fish. Student's unpaired *t*-test, mean ± SEM, ****$P < 0.0001$. Scale bar: 100 μm.

Angiogenesis is a process for generating new vessels from pre-existing vessels during development,[99] which gradually decreased and is suppressed in mature vessels, especially in arteries.[100] Here we provide evidence that angiogenic genes (*ANGPT2*, *APLN*) and pathway were ectopically enriched in the ECs of IA. ANGPT2 belongs to the angiopoietin/TIE signaling pathway, which is found to function through inhibiting ANGPT1-induced TIE2 phosphorylation.[69] Physiologically, ANGPT2 is highly expressed in angiogenic ECs, and its dysregulation had been found to implicate in diverse vascular malformations, notably in capillary malformation (CM), cerebral cavernous malformations (CCMs), hereditary hemorrhagic telangiectasia (HHT) and arteriovenous malformations (AVMs).[101–104] Several studies have proven that the above pathological conditions may come from the ANGPT2 induced EC destabilization, immune cell infiltration, ECM degradation, pericyte detachment, and increased vascular permeability.[105,106] However, on the contrary, a latest study suggested the protective role of ANGPT2 in maintaining stability of cerebral vessels.[39] Therefore, the function of ANGPT2 is still debated. In addition, for peripheral aneurysms, Hongyou *et al.* demonstrated that the Angpt2 limits the occurrence of abdominal aortic aneurysm (AAA) and atherosclerosis in a mouse model associated with reduced angiogenesis and inflammation.[107] Jonathan *et al.* found the serum ANGPT2 is elevated in men with AAA and predicted a higher cardiovascular motality.[108] However, the role of ANGPT2 in IA has not been reported yet. As we observed the elevated expression of *ANGPT2*, we therefore try to investigate its roles within ECs in IA. The present study used the well-established vertebrate model of zebrafish and found that EC-specific expression of *angpt2a* caused IA-like vascular dilation and EC alterations (*Figure 4* and Supplementary material online, *Figure S8A*). We also introduced a novel genetic model of IA mimicking the arterial abnormalities in human IAs, which can be used for long-term *in vivo* exploration of IA pathogenesis at both molecular and cellular level. And we found the phenotypes of our IA-like zebrafish can be partially rescued by knocking down of *angpt2a* (*Figures 5* and *6*). Therefore, our data support the destabilizing role of ANGPT2 in ECs. APLN, also being a marker for tip cells, has pivotal roles in developmental angiogenesis, especially in regulating ECs migration, division, and apoptosis.[109,110] And similarly, though the implication of APLN in IA have not been addressed yet, a critical

protective role of APLN in atherosclerosis and AAA formation had been drawn.[111,112] Here, we found the EC-specific expression of *apln* in zebrafish causes no significant vascular changes, while a similar alleviation of arterial dilation in *apln* knockdown IA-like zebrafish (*Figure 6B* and *C*). These results suggest that *ANGPT2* and *APLN* may be potential therapeutical targets for IA.

Previous studies have indicated that the inflammatory response plays a significant role in the formation, progression, and rupture of IA.[4,113] The immune response is primarily caused by infiltration of immune cells, resulting in damage to vascular cells, and degradation and remodeling of the ECM.[61] The altered homeostasis of vascular microenvironment triggers cascade response of inflammation in the vascular wall.[114] Here we also observed the increased infiltration of immune cells in IA tissues, including T/NK cells, B cells, macrophages and dendritic cells. The T/NK cells rank the highest both in the abundance of immune cell population and increased proportions. Previous study indicates the function of T cells are dispensable for IA formation. However, the heterogeneity of T cells is still unknown in IA.[115] In this study, we explored the heterogeneity of T cells and found that there is an increased presence of effector-like T cells in IA. These T cells expressed high levels of cytotoxic cytokines and exhaustion-related transcription factors, while the populations of memory and naive T cells decreased (Supplementary material online, *Figure S5F–I*). Macrophages are thought to be the first immune cells to encounter stimuli and are the primary producers of reactive oxygen species that promote enzymatic reactions and damage the blood vessel wall.[65,116] In contrast to T cell deletion, depletion of macrophages significantly reduced the incidence of IAs.[61] In the brain, macrophages can be activated into two distinct phenotypes: the pro-inflammatory M1-like or the anti-inflammatory M2-like.[117] Our findings show that M1-like macrophages are enriched in IA tissues, indicating the pro-inflammatory polarization of macrophages in the pathophysiological process. We also performed an analysis using the signature AddModuleScore, and we observed a striking correlation between the inflammatory score of myeloid cells and the angiogenic score of ECs (Supplementary material online, *Figure S7B*). This finding suggests a potential link between angiogenesis and the immune response, which could contribute to our understanding of the pathogenesis of IA.

However, it is also essential to acknowledge certain limitations within this research. First, given that endovascular interventions have become the primary treatment for IAs, the availability of human samples suitable for scRNA-seq analysis is limited. This challenge is further compounded by difficulties in the preparation of fresh single-cell suspensions. Therefore, future studies should strive to incorporate IA samples from a wider range of arterial positions and diverse sample sizes. This approach will facilitate comparisons among distinct disease conditions, enhancing our overall understanding of IA. Furthermore, it's worth noting that we observed a potential imbalance among our collected IA samples. For instance, the enrichment of *ANGPT2* and *APLN* expression in ECs of IAs appeared to be primarily driven by patient IA2. This discrepancy may arise from genetic variations, environmental influences, or lifestyle differences between individuals, contributing to divergences in genome, expression profiles, and metabolites of biological samples. To further demonstrate the enhanced expression of *ANGPT2* and *APLN*, we conducted immunofluorescence staining in several samples from IA patients, which help to enhance the significance as the elevation of both genes had been observed in most of the IA samples. Besides, another limitation of our IA-like zebrafish model is its lack of specificity for vSMCs, as it also affects brain pericytes on the capillaries. Currently, there is no existing genetic animal model with a specific deficiency in vSMCs in arteries. Therefore, exploring novel strategies to develop such a model using different approaches holds significant value.

In all, our work provides a comprehensive analysis of the cellular compositions and transcriptome profiles of IA sample and reveals the important role of EC-intrinsic *ANGPT2* in the formation and progression of IA. These findings have important implications for our understanding of the disease and provide a potential target for future intervention.

Translational perspective

The current study elucidates the dynamic cellular compositions and transcriptome profiles in human intracranial aneurysm (IA) and the control artery, which provides important resources for future studies of the molecular mechanisms underlying IA formation and progression. Especially, the obtaining of high-quality and high-quantity endothelial cells from IA patients, permits the uncovering of their heterogeneity. In addition, our results demonstrate that inhibition of *ANGPT2* may hold potential therapeutic benefits for IA interventions.

Supplementary material

Supplementary material is available at *Cardiovascular Research* online.

Authors' Contributions

J.L., J.D., W.Z., and G.Y. conceptualized and supervised the study; J.L. designed the experiments. G.Y. organized human tissue samples and performed the pathological staining. H.Z., J.L., H.Zi., and M.L. analysed the scRNA-seq data. J.L. and H.Zi. contributed to the generation and characterization of IA zebrafish model. H.Z. carried out the EC-specific screening and crispant experiments in IA zebrafish and analysed the data. J.L., H.Zi. and H.Z. designed and generated the plasmids for zebrafish studies. P.Li., J.S., P.Liu., K.Q., S.L., and Y.L. helped with the human sample collection. G.Y., Q.A. and T.Q. performed human tissue dissociation. M.L. carried out the RNAscope experiments. H.Z., J.L., and G.Y. wrote the manuscript with inputs from J.D. and W.Z.

Acknowledgements

The authors thank the OE Biotech CO. Ltd. (Shanghai, China) for providing single-cell RNA sequencing, Yongbing Ba and Lian Li for assistance with bioinformatics analysis. The *graphical abstract* was created with BioRender.com.

Conflict of interest: none declared.

Funding

This study was supported by the National Natural Science Foundation of China (No. 82330039 to W.Z., No. 82171311 to W.Z., No. 82171314 to G.Y., No. 82271339 to P.Liu., No. 82201466 to S.L.), Shanghai Excellent Academic Leaders Program (No. 21XD1400600 to W.Z.), Special Clinical Research Project in Health Industry of Shanghai Municipal Health Commission (No. 20224Y0072 to P.L.), Clinical Research Plan of SHDC (No. SHDC2020CR2034B to W.Z., No. SHDC2020CR4033 to K.Q.), Shanghai Science and Technology Commission Project (No. 23ZR1408700 to K.Q.), Shanghai Municipal Science and Technology Major Project (No. 2018SHZDZX01) and ZJ Lab, and CAMS Innovation Fund for Medical Sciences (CIFMS, 2019-I2M-5-008), SA-SIBS Scholarship Program (J.L.), Youth Innovation Promotion Association of Chinese Academy of Sciences (J.L.), and National Key R&D Program of China (No. 2019YFA0801603 to J.L.).

Data availability

The data that supports the conclusions of this study are available from the corresponding author upon reasonable request.

References

1. Vlak MHM, Algra A, Brandenburg R, Rinkel GJE. Prevalence of unruptured intracranial aneurysms, with emphasis on sex, age, comorbidity, country, and time period: a systematic review and meta-analysis. *Lancet Neurol* 2011;**10**:626–636.
2. Nieuwkamp DJ, Setz LE, Algra A, Linn FHH, de Rooij NK, Rinkel GJE. Changes in case fatality of aneurysmal subarachnoid haemorrhage over time, according to age, sex, and region: a meta-analysis. *Lancet Neurol* 2009;**8**:635–642.
3. Xu Z, Rui Y-N, Hagan JP, Kim DH. Intracranial aneurysms: pathology, genetics, and molecular mechanisms. *Neuromolecular Med* 2019;**21**:325–343.
4. Etminan N, Rinkel GJ. Unruptured intracranial aneurysms: development, rupture and preventive management. *Nat Rev Neurol* 2016;**12**:699–713.
5. Wen L, Tang F. Boosting the power of single-cell analysis. *Nat Biotechnol* 2018;**36**:408–409.
6. Lukowski SW, Patel J, Andersen SB, Sim S-L, Wong HY, Tay J, Winkler I, Powell JE, Khosrotehrani K. Single-cell transcriptional profiling of aortic endothelium identifies a hierarchy from endovascular progenitors to differentiated cells. *Cell Rep* 2019;**27**:2748–2758.e3.
7. Li Y, Ren P, Dawson A, Vasquez HG, Ageedi W, Zhang C, Luo W, Chen R, Li Y, Kim S, Lu HS, Cassis LA, Coselli JS, Daugherty A, Shen YH, LeMaire SA. Single-cell transcriptome analysis reveals dynamic cell populations and differential gene expression patterns in control and aneurysmal human aortic tissue. *Circulation* 2020;**142**:1374–1388.
8. Davis FM, Tsoi LC, Ma F, Wasikowski R, Moore BB, Kunkel SL, Gudjonsson JE, Gallagher KA. Single-cell transcriptomics reveals dynamic role of smooth muscle cells and enrichment of immune cell subsets in human abdominal aortic aneurysms. *Ann Surg* 2022;**276**:511–521.
9. Martinez AN, Tortelote GG, Pascale CL, McCormack IG, Nordham KD, Suder NJ, Couldwell MW, Dumont AS. Single-cell transcriptome analysis of the circle of Willis in a mouse cerebral aneurysm model. *Stroke* 2022;**53**:2647–2657.
10. Wen D, Wang X, Chen R, Li H, Zheng J, Fu W, Zhang T, Yang M, You C, Ma L. Single-cell RNA sequencing reveals the pathogenic relevance of intracranial atherosclerosis in blood blister-like aneurysms. *Front Immunol* 2022;**13**:927125.
11. Butler A, Hoffman P, Smibert P, Papalexi E, Satija R. Integrating single-cell transcriptomic data across different conditions, technologies, and species. *Nat Biotechnol* 2018;**36**:411–420.
12. Haghverdi L, Lun ATL, Morgan MD, Marioni JC. Batch effects in single-cell RNA-Sequencing data are corrected by matching mutual nearest neighbors. *Nat Biotechnol* 2018;**36**:421–427.
13. Trapnell C, Cacchiarelli D, Grimsby J, Pokharel P, Li S, Morse M, Lennon NJ, Livak KJ, Mikkelsen TS, Rinn JL. The dynamics and regulators of cell fate decisions are revealed by pseudotemporal ordering of single cells. *Nat Biotechnol* 2014;**32**:381–386.
14. Aibar S, González-Blas CB, Moerman T, Huynh-Thu VA, Imrichova H, Hulselmans G, Rambow F, Marine J-C, Geurts P, Aerts J, van den Oord J, Atak ZK, Wouters J, Aerts S. SCENIC: single-cell regulatory network inference and clustering. *Nat Methods* 2017;**14**:1083–1086.
15. Suo S, Zhu Q, Saadatpour A, Fei L, Guo G, Yuan G-C. Revealing the critical regulators of cell identity in the mouse cell atlas. *Cell Rep* 2018;**25**:1436–1445.e3.
16. Hänzelmann S, Castelo R, Guinney J. GSVA: gene set variation analysis for microarray and RNA-seq data. *BMC Bioinformatics* 2013;**14**:7.
17. Wu Y, Yang S, Ma J, Chen Z, Song G, Rao D, Cheng Y, Huang S, Liu Y, Jiang S, Liu J, Huang X, Wang X, Qiu S, Xu J, Xi R, Bai F, Zhou J, Fan J, Zhang X, Gao Q. Spatiotemporal immune landscape of colorectal cancer liver metastasis at single-cell level. *Cancer Discov* 2022;**12**:134–153.
18. DeTomaso D, Jones MG, Subramaniam M, Ashuach T, Ye CJ, Yosef N. Functional interpretation of single cell similarity maps. *Nat Commun* 2019;**10**:4376.
19. McDavid A, Finak G, Chattopadyay PK, Dominguez M, Lamoreaux L, Ma SS, Roederer M, Gottardo R. Data exploration, quality control and testing in single-cell qPCR-based gene expression experiments. *Bioinformatics* 2013;**29**:461–467.
20. Jin S, Guerrero-Juarez CF, Zhang L, Chang I, Ramos R, Kuan C-H, Myung P, Plikus MV, Nie Q. Inference and analysis of cell-cell communication using CellChat. *Nat Commun* 2021;**12**:1088.
21. Kusumbe AP, Ramasamy SK, Starsichova A, Adams RH. Sample preparation for high-resolution 3D confocal imaging of mouse skeletal tissue. *Nat Protoc* 2015;**10**:1904–1914.
22. Lorent K, Moore JC, Siekmann AF, Lawson N, Pack M. Reiterative use of the notch signal during zebrafish intrahepatic biliary development. *Dev Dynam* 2010;**239**:855–864.
23. Akitake CM, Macurak M, Halpern ME, Goll MG. Transgenerational analysis of transcriptional silencing in zebrafish. *Dev Biol* 2011;**352**:191–201.
24. Matthews M, Varga ZM. Anesthesia and euthanasia in zebrafish. *ILAR J* 2012;**53**:192–204.
25. Zi H, Peng X, Cao J, Xie T, Liu T, Li H, Bu J, Du J, Li J. Piezo1-dependent regulation of pericyte proliferation by blood flow during brain vascular development. *Cell Rep* 2024;**43**:113652.
26. Li W, Tran V, Shaked I, Xue B, Moore T, Lightle R, Kleinfeld D, Awad IA, Ginsberg MH. Abortive intussusceptive angiogenesis causes multi-cavernous vascular malformations. *Elife* 2021;**10**:e62155.
27. Susaki EA, Tainaka K, Perrin D, Yukinaga H, Kuno A, Ueda HR. Advanced CUBIC protocols for whole-brain and whole-body clearing and imaging. *Nat Protoc* 2015;**10**:1709–1727.
28. Chalouhi N, Hoh BL, Hasan D. Review of cerebral aneurysm formation, growth, and rupture. *Stroke* 2013;**44**:3613–3622.
29. Zhou Y, Zhou B, Pache L, Chang M, Khodabakhshi AH, Tanaseichuk O, Benner C, Chanda SK. Metascape provides a biologist-oriented resource for the analysis of systems-level datasets. *Nat Commun* 2019;**10**:1523.
30. Hilfiker-Kleiner D, Hilfiker A, Kaminski K, Schaefer A, Park JK, Michel K, Quint A, Yaniv M, Weitzman JB, Drexler H. Lack of JunD promotes pressure overload-induced apoptosis, hypertrophic growth, and angiogenesis in the heart. *Circulation* 2005;**112**:1470–1477.
31. Renoux F, Stellato M, Haftmann C, Vogetseder A, Huang R, Subramaniam A, Becker MO, Blyszczuk P, Becher B, Distler JHW, Kania G, Boyman O, Distler O. The AP1 transcription factor Fosl2 promotes systemic autoimmunity and inflammation by repressing Treg development. *Cell Rep* 2020;**31**:107826.
32. Wan X, Guan S, Hou Y, Qin Y, Zeng H, Yang L, Qiao Y, Liu S, Li Q, Jin T, Qiu Y, Liu M. FOSL2 promotes VEGF-independent angiogenesis by transcriptionally activating Wnt5a in breast cancer-associated fibroblasts. *Theranostics* 2021;**11**:4975–4991.
33. Takeshita K, Satoh M, Ii M, Silver M, Limbourg FP, Mukai Y, Rikitake Y, Radtke F, Gridley T, Losordo DW, Liao JK. Critical role of endothelial Notch1 signaling in postnatal angiogenesis. *Circ Res* 2007;**100**:70–78.
34. Al Haj Zen A, Oikawa A, Bazan-Peregrino M, Meloni M, Emanueli C, Madeddu P. Inhibition of delta-like-4-mediated signaling impairs reparative angiogenesis after ischemia. *Circ Res* 2010;**107**:283–293.
35. Chen F, Bai J, Li W, Mei P, Liu H, Li L, Pan Z, Wu Y, Zheng J. RUNX3 suppresses migration, invasion and angiogenesis of human renal cell carcinoma. *PLoS One* 2013;**8**:e56241.
36. Kim BR, Kang MH, Kim JL, Na YJ, Park SH, Lee SI, Kang S, Joung SY, Lee SY, Lee DH, Min BW, Oh SC. RUNX3 inhibits the metastasis and angiogenesis of colorectal cancer. *Oncol Rep* 2016;**36**:2601–2608.
37. Peng Z, Wei D, Wang L, Tang H, Zhang J, Le X, Jia Z, Li Q, Xie K. RUNX3 inhibits the expression of vascular endothelial growth factor and reduces the angiogenesis, growth, and metastasis of human gastric cancer. *Clin Cancer Res* 2006;**12**:6386–6394.
38. Winkler EA, Kim CN, Ross JM, Garcia JH, Gil E, Oh I, Chen LQ, Wu D, Catapano JS, Raygor K, Narsinh K, Kim H, Weinsheimer S, Cooke DL, Walcott BP, Lawton MT, Gupta N, Zlokovic BV, Chang EF, Abla AA, Lim DA, Nowakowski TJ. A single-cell atlas of the normal and malformed human brain vasculature. *Science* 2022;**375**:eabi7377.
39. Mae MA, He L, Nordling S, Vazquez-Liebanas E, Nahar K, Jung B, Li X, Tan BC, Chin Foo J, Cazenave-Gassiot A, Wenk MR, Zarb Y, Lavina B, Quaggin SE, Jeansson M, Gu C, Silver DL, Vanlandewijck M, Butcher EC, Keller A, Betsholtz C. Single-cell analysis of blood-brain barrier response to pericyte loss. *Circ Res* 2021;**128**:e46–e62.
40. Helker CS, Eberlein J, Wilhelm K, Sugino T, Malchow J, Schuermann A, Baumeister S, Kwon HB, Maischein HM, Potente M, Herzog W, Stainier DY. Apelin signaling drives vascular endothelial cells toward a pro-angiogenic state. *Elife* 2020;**9**:e55589.
41. del Toro R, Prahst C, Mathivet T, Siegfried G, Kaminker JS, Larrivee B, Breant C, Duarte A, Takakura N, Fukamizu A, Penninger J, Eichmann A. Identification and functional analysis of endothelial tip cell-enriched genes. *Blood* 2010;**116**:4025–4033.
42. Vanlandewijck M, He L, Mäe MA, Andrae J, Ando K, Del Gaudio F, Nahar K, Lebouvier T, Laviña B, Gouveia L, Sun Y, Raschperger E, Räsänen M, Zarb Y, Mochizuki N, Keller A, Lendahl U, Betsholtz C. A molecular atlas of cell types and zonation in the brain vasculature. *Nature* 2018;**554**:475–480.
43. Mathai SK, Pedersen BS, Smith K, Russell P, Schwarz MI, Brown KK, Steele MP, Loyd JE, Crapo JD, Silverman EK, Nickerson D, Fingerlin TE, Yang IV, Schwartz DA. Desmoplakin variants are associated with idiopathic pulmonary fibrosis. *Am J Respir Crit Care Med* 2016;**193**:1151–1160.
44. Osuka S, Zhu D, Zhang Z, Li C, Stackhouse CT, Sampetrean O, Olson JJ, Gillespie GY, Saya H, Willey CD, Van Meir EG. N-cadherin upregulation mediates adaptive radioresistance in glioblastoma. *J Clin Invest* 2021;**131**:e136098.
45. Welcker D, Stein C, Feitosa NM, Armistead J, Zhang J-L, Lütke S, Kleinridders A, Brüning JC, Eming SA, Sengle G, Niehoff A, Bloch W, Hammerschmidt M. Hemicentin-1 is an essential extracellular matrix component of the dermal-epidermal and myotendinous junctions. *Sci Rep* 2021;**11**:17926.
46. Li X, Tu L, Murphy PG, Kadono T, Steeber DA, Tedder TF. CHST1 and CHST2 sulfotransferase expression by vascular endothelial cells regulates shear-resistant leukocyte rolling via L-selectin. *J Leukoc Biol* 2001;**69**:565–574.
47. Bagley RG, Rouleau C, Weber W, Mehraein K, Smale R, Curiel M, Callahan M, Roy A, Boutin P, St Martin T, Nacht M, Teicher BA. Tumor endothelial marker 7 (TEM-7): a novel target for antiangiogenic therapy. *Microvasc Res* 2011;**82**:253–262.
48. Wyder L, Suply T, Ricoux B, Billy E, Schnell C, Baumgarten BU, Maira SM, Koelbing C, Ferretti M, Kinzel B, Müller M, Seuwen K, Ludwig M-G. Reduced pathological angiogenesis and tumor growth in mice lacking GPR4, a proton sensing receptor. *Angiogenesis* 2011;**14**:533–544.
49. Hill RA, Tong L, Yuan P, Murikinati S, Gupta S, Grutzendler J. Regional blood flow in the normal and ischemic brain is controlled by arteriolar smooth muscle cell contractility and not by capillary pericytes. *Neuron* 2015;**87**:95–110.
50. Huang R, Merrilees MJ, Braun K, Beaumont B, Lemire J, Clowes AW, Hinek A, Wight TN. Inhibition of versican synthesis by antisense alters smooth muscle cell phenotype and induces elastic fiber formation in vitro and in neointima after vessel injury. *Circ Res* 2006;**98**:370–377.
51. Nie X, Shen C, Tan J, Wu Z, Wang W, Chen Y, Dai Y, Yang X, Ye S, Chen J, Bian J-S. Periostin: a potential therapeutic target for pulmonary hypertension? *Circ Res* 2020;**127**:1138–1152.
52. Wu J, Subbaiah KCV, Xie LH, Jiang F, Khor E-S, Mickelsen D, Myers JR, Tang WHW, Yao P. Glutamyl-prolyl-tRNA synthetase regulates proline-rich pro-fibrotic protein synthesis during cardiac fibrosis. *Circ Res* 2020;**127**:827–846.
53. Veith C, Vartürk-Özcan I, Wujak M, Hadzic S, Wu C-Y, Knoepp F, Kraut S, Petrovic A, Gredic M, Pak O, Brosien M, Heimbrodt M, Wilhelm J, Weisel FC, Malkmus K, Schäfer

K, Gall H, Tello K, Kosanovic D, Sydykov A, Sarybaev A, Günther A, Brandes RP, Seeger W, Grimminger F, Ghofrani HA, Schermuly RT, Kwapiszewska G, Sommer N, Weissmann N. SPARC, a novel regulator of vascular cell function in pulmonary hypertension. *Circulation* 2022;**145**:916–933.
54. Liu P, Shi Y, Fan Z, Zhou Y, Song Y, Liu Y, Yu G, An Q, Zhu W. Inflammatory smooth muscle cells induce endothelial cell alterations to influence cerebral aneurysm progression via regulation of integrin and VEGF expression. *Cell Transplant* 2019;**28**:713–722.
55. Johnson KA, Polewski M, Terkeltaub RA. Transglutaminase 2 is central to induction of the arterial calcification program by smooth muscle cells. *Circ Res* 2008;**102**:529–537.
56. Zhu Y, Ji JJ, Wang XD, Sun XJ, Li M, Wei Q, Ren LQ, Liu NF. Periostin promotes arterial calcification through PPARgamma-related glucose metabolism reprogramming. *Am J Physiol Heart Circ Physiol* 2021;**320**:H2222–H2239.
57. Barbier M, Gross MS, Aubart M, Hanna N, Kessler K, Guo DC, Tosolini L, Ho-Tin-Noe B, Regalado E, Varret M, Abifadel M, Milleron O, Odent S, Dupuis-Girod S, Faivre L, Edouard T, Dulac Y, Busa T, Gouya L, Milewicz DM, Jondeau G, Boileau C. MFAP5 loss-of-function mutations underscore the involvement of matrix alteration in the pathogenesis of familial thoracic aortic aneurysms and dissections. *Am J Hum Genet* 2014;**95**:736–743.
58. Pilecki B, de Carvalho P, Kirketerp-Moller KL, Schlosser A, Kejling K, Dubik M, Madsen NP, Stubbe J, Hansen PBL, Andersen TL, Moeller JB, Marcussen N, Azevedo V, Hvidsten S, Baun C, Shi GP, Lindholt JS, Sorensen GL. MFAP4 deficiency attenuates angiotensin II-induced abdominal aortic aneurysm formation through regulation of macrophage infiltration and activity. *Front Cardiovasc Med* 2021;**8**:764337.
59. Schlosser A, Pilecki B, Hemstra LE, Kejling K, Kristmannsdottir GB, Wulf-Johansson H, Moeller JB, Fuchtbauer EM, Nielsen O, Kirketerp-Moller K, Dubey LK, Hansen PB, Stubbe J, Wrede C, Hegermann J, Ochs M, Rathkolb B, Schrewe A, Bekeredjian R, Wolf E, Gailus-Durner V, Fuchs H, Hrabe de Angelis M, Lindholt JS, Holmskov U, Sorensen GL. MFAP4 promotes vascular smooth muscle migration, proliferation and accelerates neointima formation. *Arterioscler Thromb Vasc Biol* 2016;**36**:122–133.
60. Zhang L, Kundu S, Feenstra T, Li X, Jin C, Laaniste L, El Hassan TE, Ohlin KE, Yu D, Olofsson T, Olsson AK, Ponten F, Magnusson PU, Nilsson KF, Essand M, Smits A, Dieterich LC, Dimberg A. Pleiotrophin promotes vascular abnormalization in gliomas and correlates with poor survival in patients with astrocytomas. *Sci Signal* 2015;**8**:ra125.
61. Kanematsu Y, Kanematsu M, Kurihara C, Tada Y, Tsou T-L, van Rooijen N, Lawton MT, Young WL, Liang EI, Nuki Y, Hashimoto T. Critical roles of macrophages in the formation of intracranial aneurysm. *Stroke* 2011;**42**:173–178.
62. Muhammad S, Chaudhry SR, Dobreva G, Lawton MT, Niemelä M, Hänggi D. Vascular macrophages as therapeutic targets to treat intracranial aneurysms. *Front Immunol* 2021;**12**:630381.
63. Dick SA, Wong A, Hamidzada H, Nejat S, Nechanitzky R, Vohra S, Mueller B, Zaman R, Kantores C, Aronoff L, Momen A, Nechanitzky D, Li WY, Ramachandran P, Crome SQ, Becher B, Cybulsky MI, Billia F, Keshavjee S, Mital S, Robbins CS, Mak TW, Epelman S. Three tissue resident macrophage subsets coexist across organs with conserved origins and life cycles. *Sci Immunol* 2022;**7**:eabf7777.
64. Bruemmer D, Collins AR, Noh G, Wang W, Territo M, Arias-Magallona S, Fishbein MC, Blaschke F, Kintscher U, Graf K, Law RE, Hsueh WA. Angiotensin II-accelerated atherosclerosis and aneurysm formation is attenuated in osteopontin-deficient mice. *J Clin Invest* 2003;**112**:1318–1331.
65. Tang H, Luo Y, Zuo Q, Wang C, Huang Q, Zhao R, Liu J. Current understanding of the molecular mechanism between hemodynamic-induced intracranial aneurysm and inflammation. *Curr Protein Pept Sci* 2019;**20**:789–798.
66. Wauters E, Van Mol P, Garg AD, Jansen S, Van Herck Y, Vanderbeke L, Bassez A, Boeckx B, Malengier-Devlies B, Timmerman A, Van Brussel T, Van Buyten T, Schepers R, Heylen E, Dauwe D, Dooms C, Gunst J, Hermans G, Meersseman P, Testelmans D, Yserbyt J, Tejpar S, De Wever W, Matthys P, Collaborators C, Neyts J, Wauters J, Qian J, Lambrechts D. Discriminating mild from critical COVID-19 by innate and adaptive immune single-cell profiling of bronchoalveolar lavages. *Cell Res* 2021;**31**:272–290.
67. Sun Y, Wu L, Zhong Y, Zhou K, Hou Y, Wang Z, Zhang Z, Xie J, Wang C, Chen D, Huang Y, Wei X, Shi Y, Zhao Z, Li Y, Guo Z, Yu Q, Xu L, Volpe G, Qiu S, Zhou J, Ward C, Sun H, YinY, Xu X, Wang X, Esteban MA, Yang H, Wang J, Dean M, Zhang Y, Liu S, Yang X, Fan J. Single-cell landscape of the ecosystem in early-relapse hepatocellular carcinoma. *Cell* 2021;**184**:404–421 e416.
68. Zhang HF, Liang GB, Zhao MG, Zhao GF, Luo YH. Regulatory T cells demonstrate significantly increased functions following stimulation with IL-2 in a Tim-3-dependent manner in intracranial aneurysms. *Int Immunopharmacol* 2018;**65**:342–347.
69. Maisonpierre PC, Suri C, Jones PF, Bartunkova S, Wiegand SJ, Radziejewski C, Compton D, McClain J, Aldrich TH, Papadopoulos N, Daly TJ, Davis S, Sato TN, Yancopoulos GD. Angiopoietin-2, a natural antagonist for Tie2 that disrupts in vivo angiogenesis. *Science* 1997;**277**:55–60.
70. Liu J, Zhang M, Dong H, Liu J, Mao A, Ning G, Cao Y, Zhang Y, Wang Q. Chemokine signaling synchronizes angioblast proliferation and differentiation during pharyngeal arch artery vasculogenesis. *Development* 2022;**149**:dev200754.
71. Janssens R, Struyf S, Proost P. Pathological roles of the homeostatic chemokine CXCL12. *Cytokine Growth Factor Rev* 2018;**44**:51–68.
72. Hasan SS, Tsaryk R, Lange M, Wisniewski L, Moore JC, Lawson ND, Wojciechowska K, Schnittler H, Siekmann AF. Endothelial Notch signalling limits angiogenesis via control of artery formation. *Nat Cell Biol* 2017;**19**:928–940.
73. Toyofuku T, Yabuki M, Kamei J, Kamei M, Makino N, Kumanogoh A, Hori M. Semaphorin-4A, an activator for T-cell-mediated immunity, suppresses angiogenesis via Plexin-D1. *EMBO J* 2007;**26**:1373–1384.
74. Figenschau SL, Knutsen E, Urbarova I, Fenton C, Elston B, Perander M, Mortensen ES, Fenton KA. ICAM1 expression is induced by proinflammatory cytokines and associated with TLS formation in aggressive breast cancer subtypes. *Sci Rep* 2018;**8**:11720.
75. Ostermann G, Weber KSC, Zernecke A, Schröder A, Weber C. JAM-1 is a ligand of the beta(2) integrin LFA-1 involved in transendothelial migration of leukocytes. *Nat Immunol* 2002;**3**:151–158.
76. Thompson JW, Elwardany O, McCarthy DJ, Sheinberg DL, Alvarez CM, Nada A, Snelling BM, Chen SH, Sur S, Starke RM. In vivo cerebral aneurysm models. *Neurosurg Focus* 2019;**47**:E20.
77. Rombouts KB, van Merrienboer TAR, Ket JCF, Bogunovic N, van der Velden J, Yeung KK. The role of vascular smooth muscle cells in the development of aortic aneurysms and dissections. *Eur J Clin Invest* 2022;**52**:e13697.
78. Thompson RW, Liao S, Curci JA. Vascular smooth muscle cell apoptosis in abdominal aortic aneurysms. *Coron Artery Dis* 1997;**8**:623–631.
79. Lopez-Candales A, Holmes DR, Liao S, Scott MJ, Wickline SA, Thompson RW. Decreased vascular smooth muscle cell density in medial degeneration of human abdominal aortic aneurysms. *Am J Pathol* 1997;**150**:993–1007.
80. Lu H, Du W, Ren L, Hamblin MH, Becker RC, Chen YE, Fan Y. Vascular smooth muscle cells in aortic aneurysm: from genetics to mechanisms. *J Am Heart Assoc* 2021;**10**:e023601.
81. Ando K, Wang W, Peng D, Chiba A, Lagendijk AK, Barske L, Crump JG, Stainier DYR, Lendahl U, Koltowska K, Hogan BM, Fukuhara S, Mochizuki N, Betsholtz C. Peri-arterial specification of vascular mural cells from naive mesenchyme requires Notch signaling. *Development* 2019;**146**:dev165589.
82. Olson LE, Soriano P. PDGFRbeta signaling regulates mural cell plasticity and inhibits fat development. *Dev Cell* 2011;**20**:815–826.
83. Ando K, Shih YH, Ebarasi L, Grosse A, Portman D, Chiba A, Mattonet K, Gerri C, Stainier DYR, Mochizuki N, Fukuhara S, Betsholtz C, Lawson ND. Conserved and context-dependent roles for pdgfrb signaling during zebrafish vascular mural cell development. *Dev Biol* 2021;**479**:11–22.
84. Karasozen Y, Osbun JW, Parada CA, Busald T, Tatman P, Gonzalez-Cuyar LF, Hale CJ, Alcantara D, O'Driscoll M, Dobyns WB, Murray M, Kim LJ, Byers P, Dorschner MO, Ferreira M Jr. Somatic PDGFRB activating variants in fusiform cerebral aneurysms. *Am J Hum Genet* 2019;**104**:968–976.
85. Li J, Zhang B-B, Ren Y-G, Gu S-Y, Xiang Y-H, Du J-L. Intron targeting-mediated and endogenous gene integrity-maintaining knockin in zebrafish using the CRISPR/Cas9 system. *Cell Res* 2015;**25**:634–637.
86. Armulik A, Genove G, Mae M, Nisancioglu MH, Wallgard E, Niaudet C, He L, Norlin J, Lindblom P, Strittmatter K, Johansson BR, Betsholtz C. Pericytes regulate the blood-brain barrier. *Nature* 2010;**468**:557–561.
87. Daneman R, Zhou L, Kebede AA, Barres BA. Pericytes are required for blood-brain barrier integrity during embryogenesis. *Nature* 2010;**468**:562–566.
88. Lindahl P, Johansson BR, Leveen P, Betsholtz C. Pericyte loss and microaneurysm formation in PDGF-B-deficient mice. *Science* 1997;**277**:242–245.
89. Kim JH, Lee SR, Li LH, Park HJ, Park JH, Lee KY, Kim MK, Shin BA, Choi SY. High cleavage efficiency of a 2A peptide derived from porcine teschovirus-1 in human cell lines, zebrafish and mice. *PLoS One* 2011;**6**:e18556.
90. Nomura S, Kunitsugu I, Ishihara H, Koizumi H, Yoneda H, Shirao S, Oka F, Suzuki M. Relationship between aging and enlargement of intracranial aneurysms. *J Stroke Cerebrovasc Dis* 2015;**24**:2049–2053.
91. Parvez S, Herdman C, Beerens M, Chakraborti K, Harmer ZP, Yeh JJ, MacRae CA, Yost HJ, Peterson RT. MIC-Drop: a platform for large-scale in vivo CRISPR screens. *Science* 2021;**373**:1146–1151.
92. Sheinberg DL, McCarthy DJ, Elwardany O, Bryant JP, Luther E, Chen SH, Thompson JW, Starke RM. Endothelial dysfunction in cerebral aneurysms. *Neurosurg Focus* 2019;**47**:E3.
93. Jamous MA, Nagahiro S, Kitazato KT, Tamura T, Aziz HA, Shono M, Satoh K. Endothelial injury and inflammatory response induced by hemodynamic changes preceding intracranial aneurysm formation: experimental study in rats. *J Neurosurg* 2007;**107**:405–411.
94. Tada Y, Yagi K, Kitazato KT, Tamura T, Kinouchi T, Shimada K, Matsushita N, Nakajima N, Satomi J, Kageji T, Nagahiro S. Reduction of endothelial tight junction proteins is related to cerebral aneurysm formation in rats. *J Hypertens* 2010;**28**:1883–1891.
95. Fukuda S, Hashimoto N, Naritomi H, Nagata I, Nozaki K, Kondo S, Kurino M, Kikuchi H. Prevention of rat cerebral aneurysm formation by inhibition of nitric oxide synthase. *Circulation* 2000;**101**:2532–2538.
96. Jamous MA, Nagahiro S, Kitazato KT, Satoh K, Satomi J. Vascular corrosion casts mirroring early morphological changes that lead to the formation of saccular cerebral aneurysm: an experimental study in rats. *J Neurosurg* 2005;**102**:532–535.
97. Garcia FJ, Sun N, Lee H, Godlewski B, Mathys H, Galani K, Zhou B, Jiang X, Ng AP, Mantero J, Tsai LH, Bennett DA, Sahin M, Kellis M, Heiman M. Single-cell dissection of the human brain vasculature. *Nature* 2022;**603**:893–899.
98. Yang AC, Vest RT, Kern F, Lee DP, Agam M, Maat CA, Losada PM, Chen MB, Schaum N, Khoury N, Toland A, Calcuttawala K, Shin H, Palovics R, Shin A, Wang EY, Luo J, Gate D, Schulz-Schaeffer WJ, Chu P, Siegenthaler JA, McNerney MW, Keller A, Wyss-Coray T. A human brain vascular atlas reveals diverse mediators of Alzheimer's risk. *Nature* 2022;**603**:885–892.

99. Herbert SP, Stainier DY. Molecular control of endothelial cell behaviour during blood vessel morphogenesis. *Nat Rev Mol Cell Biol* 2011;**12**:551–564.
100. Lee H-W, Xu Y, He L, Choi W, Gonzalez D, Jin S-W, Simons M. Role of venous endothelial cells in developmental and pathologic angiogenesis. *Circulation* 2021;**144**:1308–1322.
101. Khosraviani N, Wu R, Fish JE. Angiopoietin-2: an emerging tie to pathological vessel enlargement. *Arterioscler Thromb Vasc Biol* 2022;**42**:3–5.
102. Huang L, Bichsel C, Norris AL, Thorpe J, Pevsner J, Alexandrescu S, Pinto A, Zurakowski D, Kleiman RJ, Sahin M, Greene AK, Bischoff J. Endothelial GNAQ p.R183Q increases ANGPT2 (Angiopoietin-2) and drives formation of enlarged blood vessels. *Arterioscler Thromb Vasc Biol* 2022;**42**:e27–e43.
103. Crist AM, Zhou X, Garai J, Lee AR, Thoele J, Ullmer C, Klein C, Zabaleta J, Meadows SM. Angiopoietin-2 inhibition rescues arteriovenous malformation in a Smad4 hereditary hemorrhagic telangiectasia mouse model. *Circulation* 2019;**139**:2049–2063.
104. Zhou HJ, Qin L, Zhang H, Tang W, Ji W, He Y, Liang X, Wang Z, Yuan Q, Vortmeyer A, Toomre D, Fuh G, Yan M, Kluger MS, Wu D, Min W. Erratum: endothelial exocytosis of angiopoietin-2 resulting from CCM3 deficiency contributes to cerebral cavernous malformation. *Nat Med* 2016;**22**:1502.
105. Teichert-Kuliszewska K, Maisonpierre PC, Jones N, Campbell AI, Master Z, Bendeck MP, Alitalo K, Dumont DJ, Yancopoulos GD, Stewart DJ. Biological action of angiopoietin-2 in a fibrin matrix model of angiogenesis is associated with activation of Tie2. *Cardiovasc Res* 2001;**49**:659–670.
106. Akwii RG, Sajib MS, Zahra FT, Mikelis CM. Role of angiopoietin-2 in vascular physiology and pathophysiology. *Cells* 2019;**8**:471.
107. Yu H, Moran CS, Trollope AF, Woodward L, Kinobe R, Rush CM, Golledge J. Angiopoietin-2 attenuates angiotensin II-induced aortic aneurysm and atherosclerosis in apolipoprotein E-deficient mice. *Sci Rep* 2016;**6**:35190.
108. Golledge J, Clancy P, Yeap BB, Hankey GJ, Norman PE. Increased serum angiopoietin-2 is associated with abdominal aortic aneurysm prevalence and cardiovascular mortality in older men. *Int J Cardiol* 2013;**167**:1159–1163.
109. Cox CM, D'Agostino SL, Miller MK, Heimark RL, Krieg PA. Apelin, the ligand for the endothelial G-protein-coupled receptor, APJ, is a potent angiogenic factor required for normal vascular development of the frog embryo. *Dev Biol* 2006;**296**:177–189.
110. Kang Y, Kim J, Anderson JP, Wu J, Gleim SR, Kundu RK, McLean DL, Kim J-D, Park H, Jin S-W, Hwa J, Quertermous T, Chun HJ. Apelin-APJ signaling is a critical regulator of endothelial MEF2 activation in cardiovascular development. *Circ Res* 2013;**113**:22–31.
111. Wang W, Shen M, Fischer C, Basu R, Hazra S, Couvineau P, Paul M, Wang F, Toth S, Mix DS, Poglitsch M, Gerard NP, Bouvier M, Vederas JC, Penninger JM, Kassiri Z, Oudit GY. Apelin protects against abdominal aortic aneurysm and the therapeutic role of neutral endopeptidase resistant apelin analogs. *Proc Natl Acad Sci U S A* 2019;**116**:13006–13015.
112. Chun HJ, Ali ZA, Kojima Y, Kundu RK, Sheikh AY, Agrawal R, Zheng L, Leeper NJ, Pearl NE, Patterson AJ, Anderson JP, Tsao PS, Lenardo MJ, Ashley EA, Quertermous T. Apelin signaling antagonizes Ang II effects in mouse models of atherosclerosis. *J Clin Invest* 2008;**118**:3343–3354.
113. Zeyu Z, Yuanjian F, Cameron L, Sheng C. The role of immune inflammation in aneurysmal subarachnoid hemorrhage. *Exp Neurol* 2021;**336**:113535.
114. Wu J, Chen Z-J, Liang J, Lai C-S, Li X-Y, Yang Z-J. Identifying and validating key genes mediating intracranial aneurysm rupture using weighted correlation network analysis and exploration of personalized treatment. *Ann Transl Med* 2022;**10**:1057.
115. Miyata H, Koseki H, Takizawa K, Kasuya H, Nozaki K, Narumiya S, Aoki T. T cell function is dispensable for intracranial aneurysm formation and progression. *PLoS One* 2017;**12**:e0175421.
116. Aoki T, Nishimura M, Kataoka H, Ishibashi R, Nozaki K, Hashimoto N. Reactive oxygen species modulate growth of cerebral aneurysms: a study using the free radical scavenger edaravone and p47phox(-/-) mice. *Lab Invest* 2009;**89**:730–741.
117. Xu C, Chen H, Zhou S, Sun C, Xia X, Peng Y, Zhuang J, Fu X, Zeng H, Zhou H, Cao Y, Yu Q, Li Y, Hu L, Zhou G, Yan F, Chen G, Li J. Pharmacological activation of RXR-α promotes hematoma absorption via a PPAR-γ-dependent pathway after intracerebral hemorrhage. *Neurosci Bull* 2021;**37**:1412–1426.